Journal of Electron Spectroscopy and Related Phenomena 200 (2015) 119–142

Contents lists available at ScienceDirect

Journal of Electron Spectroscopy and Related Phenomena

journal homepage: www.elsevier.com/locate/elspec

Photoelectron spectroscopy in a wide $h\nu$ region from 6 eV to 8 keV with full momentum and spin resolution

Shigemasa Suga[a,b,*], Christian Tusche[b]

[a] Institute of Scientific and Industrial Research, Osaka University, Osaka, Japan
[b] Max-Planck-Institute für Mikrostrukturphysik, Weinberg 2, 06120 Halle, Germany

ARTICLE INFO

Article history:
Available online 5 May 2015

Keywords:
PES
ARPES
SP-ARPES
Momentum microscope
Spin-filter

ABSTRACT

High resolution photoelectron spectroscopy is recognized to be a very powerful approach to study surface and bulk electronic structures of various solids by employing different photon energies ($h\nu$). In particular, angle resolved photoelectron spectroscopy (ARPES) has progressed dramatically in the last few decades providing useful information on Fermi surface (FS) topology and band dispersions.

The information of the electron spin is often decisive to fully understand the electronic properties of many material classes. However, spin-resolved studies by photoelectron spectroscopy were strongly hindered by the low detection efficiency of spin detectors. In the case of surface electronic structures, possible surface degradation with time is a serious problem to discuss intrinsic electronic effects. Therefore rather fast and high efficiency detection is required in the case of surface sensitive spin-resolved ARPES.

Two-dimensional (2D) detection is nowadays widely employed in ARPES. In the use of a conventional hemispherical deflection analyzer (HDA), one direction on the 2D detector corresponds to the binding energy E_B and the other direction to the emission angle. The novel concept of momentum microscopy, however, directly provides 2D (k_x,k_y) maps of the photoemission intensities. The reciprocal space image directly represents the cross section through the valence band structure of the sample at a selected energy. By scanning E_B, very high resolution three-dimensional $E_B(k_x,k_y)$ maps of the band-dispersion can be obtained with high efficiency.

If combined with a 2D imaging spin filter, based on electron reflection at a Au/Ir(0 0 1) surface, spin detection efficiency with orders of magnitude higher than other spin detectors is realized, opening a breakthrough in spin-resolved ARPES (SP-ARPES).

1. Introduction

Photoelectron spectroscopy (PES) is nowadays recognized to be a very powerful tool to study detailed electronic structures of various materials, which attract wide interest in both fundamental science and application [1–3]. The bulk sensitivity is, however, much less (or probing-depth is much shorter) than photon spectroscopy techniques such as photo-absorption, -reflectance, -luminescence, or resonance inelastic (soft- or hard-) X-ray scattering. The merit of PES is the freedom to select the excitation photon energy ($h\nu$) in a wide region from a few eV up to thousands of eV for exciting some particular electronic states. This freedom provides its unique capability to probe or disentangle the contributions of the complex bulk and surface electronic components. Since the photon has a well defined wave-vector $\boldsymbol{q}$, energy $h\nu$, as well as polarization, it is relatively easy to derive useful information on the initial electronic states owing to the energy- and momentum-conservation rules and optical selection rules. Angle-resolved photoelectron spectroscopy (ARPES) has become a standard methodology to study band structures in solids, revealing their dispersions in the momentum space. Since the detection efficiency of ARPES is much lower than that of angle-averaged photoelectron spectroscopy, ARPES in a wide momentum ($\mathbf{k}$) region with high resolutions in both energy and momentum spaces is not easy, particularly in the cases of reactive surfaces. In order to overcome this difficulty, simultaneous two-dimensional (2D) momentum ($\mathbf{k}$) mapping depending on the binding energy in the form of $E_B(k_x,k_y)$ was developed in recent years. The concept of this novel technique, called momentum microscopy, corresponding instruments and some examples are described later in Section 7.

* Corresponding author at: Institute of Scientific and Industrial Research, Osaka University, Ibaraki, Osaka 567-0047, Japan.
E-mail address: ssmsuga@gmail.com (S. Suga).

http://dx.doi.org/10.1016/j.elspec.2015.04.019
0368-2048/

The spin of the electron is in many cases decisive to fully understand the origin of individual electronic structures in solids. The detection efficiency of the photoelectron spin, however, has been very low for decades because of the low figure of merit f_0 in the range up to 10^{-4} of the spin detector [4] such as the widely used Mott detector [5]. Though f_0 was noticeably improved in the case of the W(0 0 1)-SPLEED detector [6], still the low spin detection efficiency hindered detailed studies of spin-resolved ARPES (SP-ARPES). Very recently the development of the Fe(0 0 1)-$p(1\times1)$—O VLEED detector [7] could improve f_0 by two orders of magnitude up to $\sim10^{-2}$. These spin detectors are called single-channel spin detectors, by which only the spin at one energy and at one (k_x,k_y) point can be detected before changing (k_x,k_y), for example, by rotating the sample. One can call this zero-dimensional (0D) measurement and such a spin detection as zero-dimensional 0D-spin detection. The recent development of imaging spin filters allowed simultaneous spin detection at all (k_x,k_y) covered by a 2D detector, providing the information on spin-polarization $P_s(E_B(k_x,k_y))$ at a certain E_B [8]. Then this technique is called 2D-spin detection. One can obtain the full 2D-SP-ARPES with much higher efficiency than the preceding 0D-SP-ARPES technique as explained in Section 8.

ARPES and SP-ARPES are of course partially possible by use of conventional ARPES instruments with 2D detectors and 0D spin detection instruments, respectively, in a limited E_B range or limited (k_x,k_y) region. However, numbers of data points as well as the energy- and momentum-resolution are limited because of the low detection efficiency. Therefore complete 2D band dispersions $E_B(k_x,k_y)$ and spin polarization maps $P_s(E_B(k_x,k_y))$ are very difficult to obtain. Measurements of a well defined surface region with the best sample quality is rather important for reliable discussion of the global electronic structures. When the sample is rotated to cover a wide (k_x,k_y) region, the area under the incident light illumination may not be fixed and the photoelectrons from different areas on the sample surface will be detected. Moreover the intensity normalization at all (k_x,k_y) becomes less accurate because the E_B dependence of the intensity at each (k_x,k_y) is recorded at different channels of the 2D detector of the conventional ARPES as explained later in Section 3 (Fig. 3).

Experimental 2D-ARPES and 2D-SP-ARPES, namely $E_B(k_x,k_y)$ and $P_s(E_B(k_x,k_y))$ obtained with high enough resolutions in a wide momentum space provide important information to be compared with detailed first principles band calculations and will stimulate advanced theoretical approaches. Spin polarization $P_s(E_B(k_x,k_y))$ depending upon the polarization of the excitation light and also the angle of incidence of the photon will provide detailed information on individual electronic structures. Finally the prospect of SP-ARPES will be given in Section 9.

2. Importance of soft X-ray photoelectron spectroscopy with increased bulk sensitivity

By use of synchrotron radiation from the bending magnet section of electron storage rings, it became possible to compare the photoelectron spectra measured at different $h\nu$. The utilization of undulator radiation [9–11] from the straight section with much higher brightness than the bending magnet synchrotron radiation greatly promoted the photoelectron spectroscopy. The polarization-interchange of the undulator radiation is also available to study dichroism of photoelectron emission intensity in ARPES. The tunability of $h\nu$ to the core absorption threshold energy enabled one to make resonance photoemission (RPES) studies. Resonance photoemission takes place when (1) the direct photoemission process from a valence band (Fig. 1(a)) and (2) non-radiative direct recombination process of the core hole with leaving one hole in the same valence band (Fig. 1(c)), just after the core level "resonant" excitation (Fig. 1(b)), interfere with each other. Then a Fano type resonance minimum below the core level excitation threshold $h\nu$ and a prominent resonance maximum at the threshold are often induced. As a result some particular electronic component even with only small spectral weight in the mixed valence band can be enhanced by 2 to 3 orders of magnitude and become recognizable under the resonance maximum condition.

As an example, the potential of the resonance soft X-ray photoemission was demonstrated in the case of Ce 4f states in $CeRu_2$ compared with those in $CeRu_2Si_2$ [12]. It is known that $CeRu_2$ is a strongly valence fluctuating Ce 4f system with the Kondo temperature T_K of the order of 1000 K and with the Sommerfeld (or electronic specific heat) coefficient $\gamma\sim30$ mJ/mol K^2, whereas $CeRu_2Si_2$ is a typical heavy fermion system with $T_K\sim20$ K and $\gamma\sim400$ mJ/mol K^2. Here T_K represents the hybridization strength between the 4f states and the conduction electron states. Fig. 1(d) shows the Ce 4f spectra measured under the Ce 4d–4f resonance ($h\nu\sim120$ eV) and Ce 3d–4f resonance ($h\nu\sim880$ eV) conditions. Although the 4d–4f resonance spectra are rather similar to each other in spite of the very different characters of the Ce 4f electronic states in these two typical materials, the 3d–4f resonance spectra shows much different spectral shapes. Namely, $CeRu_2Si_2$ shows a sharp peak near the Fermi level (E_F) with a broad tail to $E_B\sim4$ eV (not shown here). The noticeably different Ce 4f spectra between $CeRu_2$ and $CeRu_2Si_2$ in the 3d–4f resonance are consistent with their bulk electronic properties. Although bulk-dominated Ce 4f spectra of Ce compounds with T_K lower than 150 K (such as $CeRu_2Ge_2$ with $T_K<1$ K, CeB_6 with $T_K\sim3$ K, $CeRu_2Si_2$ with $T_K\sim20$ K, CeNi with $T_K\sim150$ K) can be well reproduced by the single impurity Anderson model using the non-crossing approximation [3,13], the bulk Ce 4f spectrum in $CeRu_2$ is largely different from these spectra. The broad bulk peak near $E_B\sim0.5$ eV in $CeRu_2$ may be most likely ascribed to the itinerant Ce 4f band structure [14]. It is thus demonstrated that careful studies are required to extract the bulk electronic components in photoelectron spectroscopy of strongly correlated electron systems such as rare earth compounds and some transition metal compounds.

Importance of the bulk sensitive photoelectron spectroscopy is not only recognized in lanthanide compounds but also in several transition metal compounds. For example, the metal-to-insulator transition (MIT) in some transition metal oxides attracts rather wide interest as for the origin of the MIT. The interplay among the on-site Coulomb repulsive energy (U: correlation energy), band width (W) and lattice distortion effects must be taken into account for proper understanding of the change of the electronic structures. Although U does not change much through the crystal up to the surface, W becomes decreased on the surface because of the reduced number of nearest neighbor atoms. Then the surface electronic states become less itinerant than in the bulk. In addition lattice distortion will induce additional effects in the case of some materials.

For example, the clear difference of the electronic structure between the bulk and surface is shown in Fig. 2 for the cases of $SrVO_3$, $Sr_{0.5}Ca_{0.5}VO_3$ and $CaVO_3$ [15] which are all metals. The occupied V 3d electronic state is nominally in the $3d^1$ (V^{4+}) configuration. Photoelectron spectra measured at $h\nu<120$ eV have shown a relatively pronounced lower Hubbard band (LHB) near $E_B\sim1.5$–1.7 eV [16,17] compared with the quasi-particle (QP) component near E_F. They are also called incoherent part and coherent part, respectively. The relatively enhanced intensity of LHB at $h\nu=21.2$ and 40.8 eV in all these three materials and in particular in $CaVO_3$ cannot be explained by theoretical band calculations and disagrees also with the results of other bulk sensitive experiments. For example transport and thermodynamic properties such as resistivity, electronic specific heat coefficient γ and paramagnetic susceptibility do not change much in these materials, but low

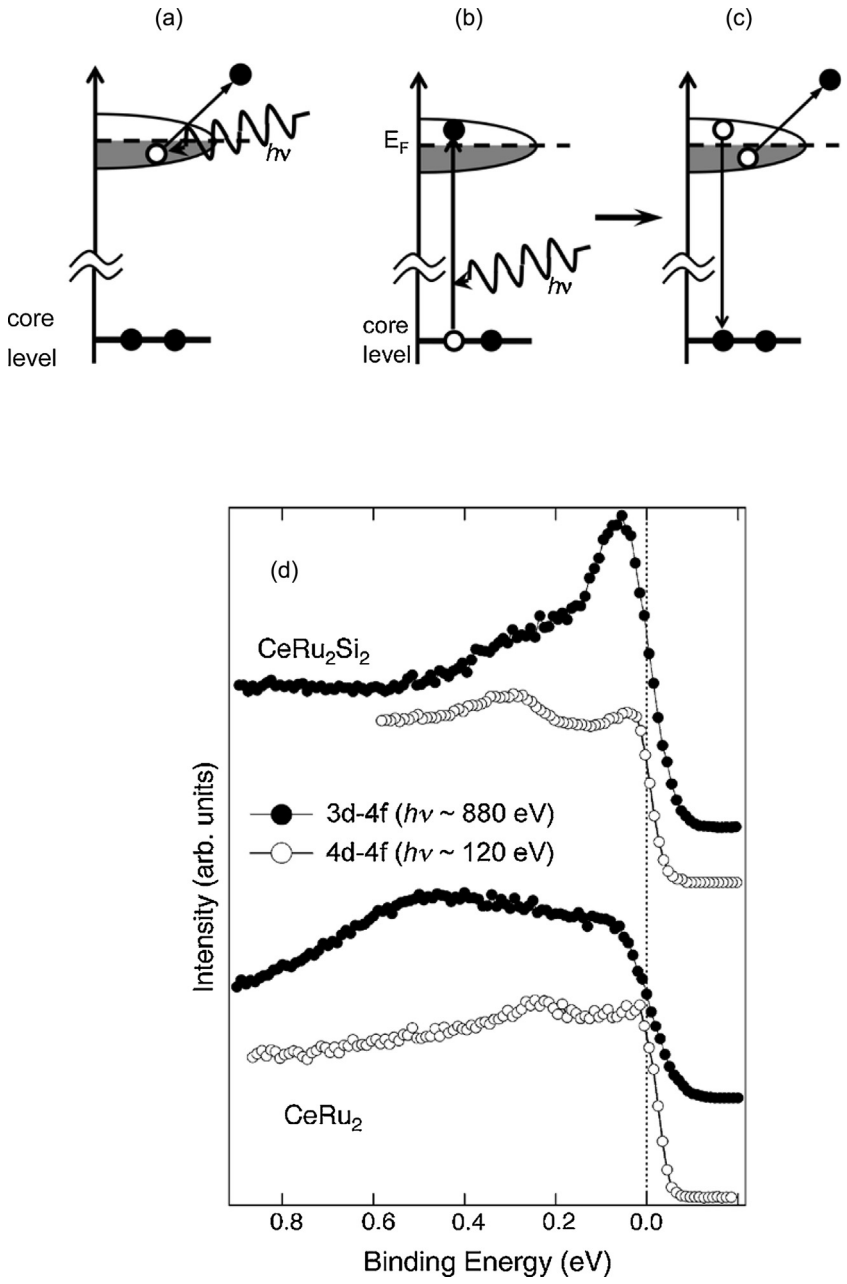

Fig. 1. Resonance photoemission spectra of $CeRu_2Si_2$ and $CeRu_2$ at the Ce 3d–4f and Ce 4d–4f absorption edges at ~20 K. Although the Ce 4d–4f resonance spectra are very similar to each other, the Ce 3d–4f spectra are very different between two materials reflecting their bulk electronic properties [12].

$h\nu$ (21.2 eV) photoelectron spectra showed much different spectral shapes depending upon the chemical composition. In addition, the QP peak intensity relative to that of LHB is very weak in $CaVO_3$ as if $CaVO_3$ is very close to the Mott transition regime.

However, spectral shapes change a lot with $h\nu$, where the relative intensity between the QP and the LHB stays almost constant among these three materials at $h\nu = 900$ eV, though it becomes drastically reduced with decreasing $h\nu$ through $h\nu = 275$, 40.8 and 21.2 eV. In addition, the reduction is most prominent in $CaVO_3$. It is possible to derive the genuine bulk spectral component from the two spectra at $h\nu = 900$ and 275 eV by employing the theoretically derived inelastic mean free path (corresponding to the effective attenuation length) of photoelectrons from the valence band as $\lambda_{mp} \sim 17$ Å and ~7 Å [18] at these $h\nu$ and assuming the thickness of the surface to be ~7.5 Å (double V—O—V length). In this case, the bulk spectral weight is estimated to be ~64 (~34) % in the experimental spectra obtained at $h\nu = 900$ (275) eV. Then the bulk V 3d spectral weight can be derived near E_F and it is confirmed to be almost equivalent among these three materials. It is thus demonstrated as the photoelectron spectroscopy in a wide $h\nu$ region, ranging over ten or hundred times, is desirable to study bulk electronic structures of strongly correlated electron systems and discriminate the bulk and surface electronic structures. It is also useful for many materials with surface reconstruction and relaxation.

Even though photoelectron spectroscopy in a wide $h\nu$ region from a few eV up to a few keV on the same sample surface might be immediately difficult, it is strongly recommended in the case of strongly correlated materials to do the measurement of valence bands at $h\nu$ beyond several hundred eV for discussing their bulk electronic structures in order to be free from possible misunderstanding of bulk physics. Several soft X-ray

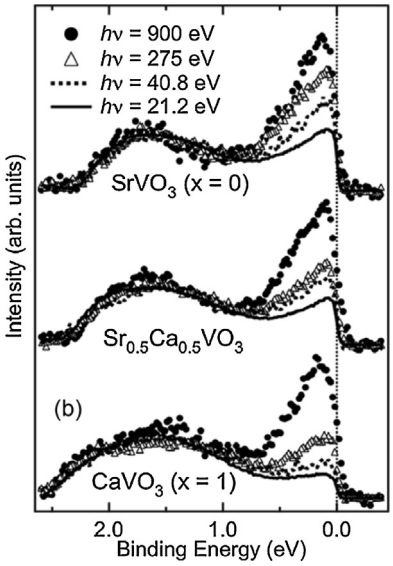

Fig. 2. Valence band photoemission spectra of $Sr_{1-x}Ca_xVO_3$. The $h\nu$ dependence of the spectra at 20 K for $x = 0$, 0.5 and 1.0 are shown. For each x, the four spectra are normalized in the region of the LHB near $E_B = 1.5$ eV. When bulk sensitivity increases from 21.2 to 900 eV, the spectra become rather similar for these three materials [15].

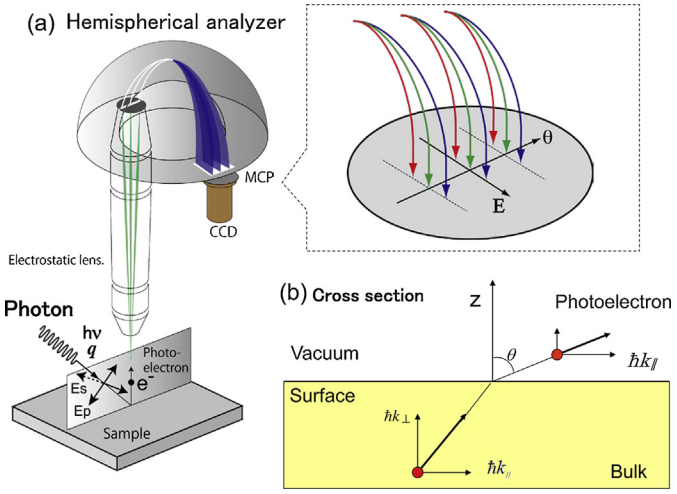

Fig. 3. Typical ARPES instrument by use of a hemispherical electron energy analyzer and a 2D detector [23,24]. The photoexcited electron in solids has the wave vector $\boldsymbol{k}$ of $k_{f||} = k_{i||} + G_{||} + q_{||}$ and $k_{f\perp} = k_{i\perp} + G_\perp - q_\perp$, where f and i stand for the final and initial states and G for the reciprocal lattice vector. The $\boldsymbol{q}$ is the wave-vector of the photon. Only $k_{||}$ (parallel to the surface) is conserved on the escape of photoelectrons into the vacuum.

undulator beam lines with (1) high brightness, (2) high resolution and high stability of $h\nu$ and (3) tunability of undulator radiation polarization are nowadays available in several synchrotron radiation facilities all over the world. Soft X-ray photoelectron spectroscopy including ARPES [9,19–22] is essentially contributing to the materials sciences of very many attractive materials under hot discussions.

3. How is the progress of angle resolved photoelectron spectroscopy

Angle resolved photoelectron spectroscopy (ARPES) is extremely useful to study the dispersions of complicated bands and reveal the Fermi surface (FS) topology of metals. This technique, first applied to semiconductors and some metals in the $h\nu$ region below ~200 eV, was later extended to the soft X-ray (SX) region in $h\nu = 200$–1000 eV in accordance with the improvement of the performance of undulator beam lines, photon-monochromators and electron analyzers [3,23]. Today, ARPES is a standard technique to study the electronic structure of various materials such as high T_c superconductors, strongly correlated electron systems, materials with phase transitions and so on. By utilizing 2D detectors, the detection efficiency is much improved in comparison with the single-channel detection. The most popular detection system is a combination of a 2D detector with a hemispherical deflection analyzer (HDA) as illustrated in Fig. 3 [24], where simultaneous multi-channel detection is feasible to cover the wide electron emission angle $\theta_{||}$ along the slit direction covering tens to hundreds of $k_{||}$ points and the other direction of the 2D detector corresponding to the different kinetic energy, or E_B, of photoelectrons. Since the narrow width of the entrance slit of the analyzer limits the detection angle $\theta_\perp$ perpendicular to the $\theta_{||}$ direction, most photoelectrons outside the entrance slit are just discarded and the detection efficiency becomes much lower than the angle integrated photoelectron spectroscopy. By rotating the sample step by step around the direction parallel to the entrance slit, a wide $\theta_\perp$ region can be covered. Then 2D $E_B(k_x,k_y)$ can be derived, in principle. But the step of $\theta_\perp$ cannot be set to a very small value because of the low efficiency of detection within a limited beam time in the synchrotron radiation laboratory and/or surface degradation. Therefore in most cases, SX-ARPES has been performed near E_F to study the Fermi surface topology and in wide E_B region to study characteristic band dispersions in high symmetry $k_{x,y}$ planes.

We have so far performed SX-ARPES on such materials as (1) 1D antiferromagnetic insulator $SrCuO_2$ [25], (2) metal-to-insulator transition (MIT) system V_6O_{13} [25], (3) low T_c triplet superconductor Sr_2RuO_4 and paramagnetic metal $Sr_{2-x}Ca_xRuO_4$ ($x = 0.2$) [26], (4) high T_c superconductors $La_{2-x}Sr_xCuO_4$ [3] and $Nd_{2-x}Ce_xCuO_4$ [27]. In all these cases the measurements were performed on cleaved surfaces. Then, clearly different results from the low $h\nu$ ARPES are observed, confirming the importance of the bulk sensitive SX-ARPES measurement.

One of the advantage of SX-ARPES is the ability to determine the k_z perpendicular to the cleaved single crystal surface with reasonable resolution owing to the longer inelastic mean free path (λ_{mp}) of the photoelectrons than the low $h\nu$ ARPES. In the case of high $h\nu$ SX-ARPES, measurements in a high-symmetry $E_B(k_{x,y})$ plane can be performed at different values of $h\nu$. Then a $h\nu$ dependent periodicity of band dispersions or the Fermi surface topology is often observed. By assuming a free electron final state, the inner potential V_0 as well as $h\nu$ dependence of k_z can be accurately determined from these oscillating behaviors owing to the increased λ_{mp} of the photoelectrons in high $h\nu$ SX-ARPES. For a constant $h\nu$, k_z changes quite a lot as a function of $k_{||}$ in the case of low $h\nu$ ARPES, but the relative variation of k_z becomes reduced in the case of SX-ARPES at high $h\nu$. This is illustrated in Fig. 4 (case of V_2O_3 cleaved surface), where the inset shows the cross section of the k space Brillouin zone (BZ) stacking normal to the cleavage plane. The ordinate corresponds to the k_z and the abscissa corresponds to $k_{||}$. It is noticed that k_z decreases for larger $|k_{||}|$ as shown by the arcs, since the probed states are located on a sphere of constant $|\mathbf{k}|$ in the reciprocal space. The arc within two radial straight lines corresponds to the $k_{||}$ region to be covered by a long entrance slit (in this case ±6°) [28]. In order to cover the full BZ, $h\nu$ must be tuned to several or many $h\nu$ values. The $h\nu$ tunability by using synchrotron radiation excitation facilitates the 3D-ARPES if enough counting rate is realized against the reduced photoionization cross sections and reasonable momentum resolution is realized for k_z in addition to k_x and k_y as addressed again in Section 7.1.

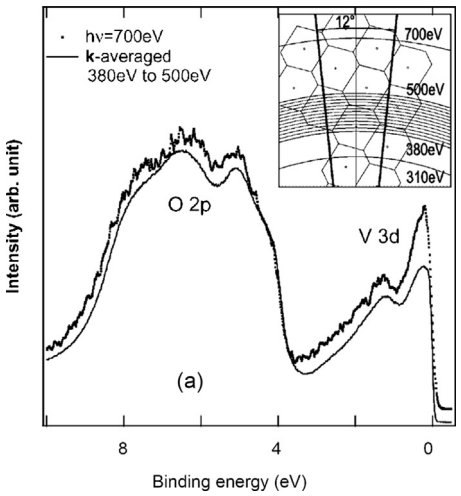

Fig. 4. Angle-averaged (or -integrated) PES spectra of paramagnetic V_2O_3 obtained at 175 K summing up the spectra measured from $h\nu$ = 380 to 500 eV in 10 eV steps. The dots show the spectrum at 700 eV. The inset shows a cross section of the BZ in the high temperature rhombohedral phase for stacking normal to the cleavage plane. The ordinate corresponds to k_z. The dense arcs show the k-region covered by the detector angular acceptance (±6°) for various $h\nu$ between 380 and 500 eV [28].

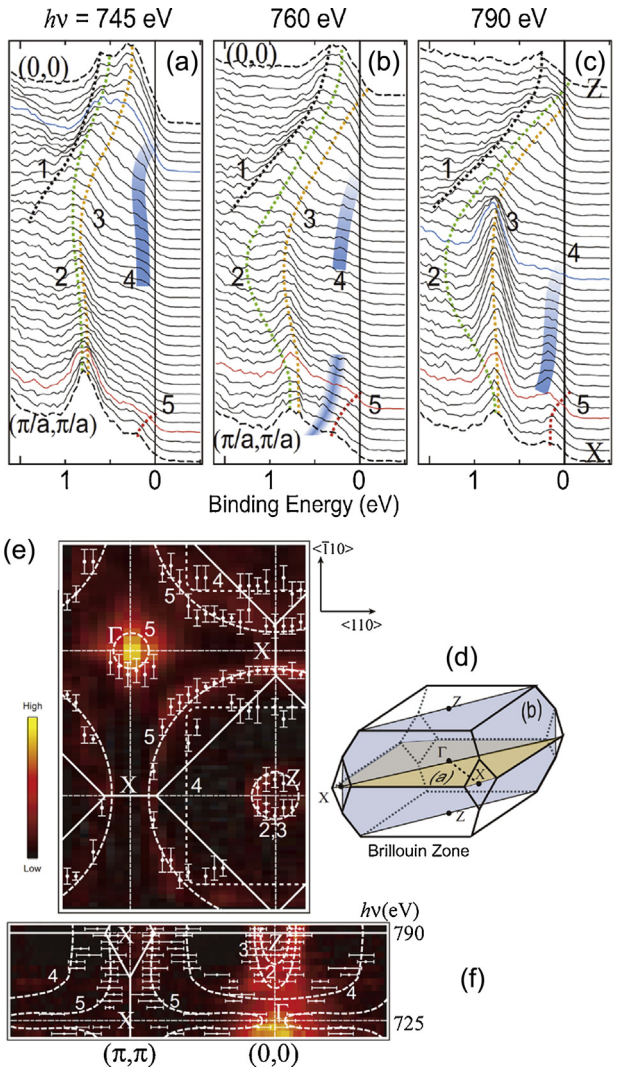

Fig. 5. $h\nu$ dependent ARPES of heavy fermion system $CeRu_2Si_2$ measured at 20 K along the (0,0)–(π/a, π/a) direction, providing partial information on 3D band dispersion. The k_z for (a)–(c) are $(4/13)(2\pi/c)$ at $h\nu$ = 745 eV, $(7/13)(2\pi/c)$ at $h\nu$ = 760 eV and $(2\pi/c)$ at $h\nu$ = 790 eV, respectively. More detailed k_z dependence is shown in (f). FS slice at $k_z \sim 0$ at $h\nu$ = 725 eV is shown in (e) [29].

Fig. 5(a)–(c) shows the band dispersions of a heavy fermion system $CeRu_2Si_2$ [29] along the (0,0)–(π,π) $k_{x,y}$ direction obtained at typical $h\nu$, where a clear dependence of the $E_B(k_{||})$ on k_z (or $h\nu$) is observed. By measuring $E_B(k_{x,y})$ at many $h\nu$, $k_z \sim 0$ is found near $h\nu$ = 725 eV. By rotating the single crystal sample, 2D band dispersions $E_B(k_x,k_y)$ in the plane containing the Γ point and the X points are obtained. From these measurements, one obtains a 2D cut through the FS in the central BZ, as shown in Fig. 4(e). By repeating the measurement of $E_B(k_{||})$ along high symmetry $k_{||}$ directions at many $h\nu$, one can evaluate the band dispersions $E_B(k_{||},k_z)$, from which the FS topology in ($k_{||}$,k_z) can be evaluated as in Fig. 4(f).

Fig. 6 shows the ARPES results of a rather itinerant 5f paramagnetic compound UB_2 [30], which has two-dimensional hexagonal AlB_2-type crystal structure. The results (a)–(c) at $h\nu$ = 500 eV correspond roughly to the plane containing A–H–L axes and those (d)–(f) at 450 eV to the plane containing Γ–K–M axes, where $V_0 \sim 12$ eV. Fig. 6(a) and (d) show the ($k_{||x}$,$k_{||y}$) FS topology derived from the intensity in the E_B region of $E_F \pm 25$ meV. The white solid lines in (a) and (d) show the FS contours derived from band calculation. Good correspondence between experimental and theoretical results are seen here. Along the H–A directions also noticeable intensity is recognized in these FS pockets in (a). These additional features may correspond to the intensity resulting from the slightly shifted k_z band component (up to 0.06–0.10 Å^{-1}), which becomes observable by the finite inelastic mean free path of photoelectrons (10–15 Å). Band dispersions along high symmetry lines are shown in (b) and (c) and (e) and (f) by taking the second energy derivatives. Calculated band dispersions are shown by red lines for comparison. The clear k_z dependence of the band dispersions suggests the general feasibility of the 3D $E_B(k_x,k_y,k_z)$ measurements by SX-ARPES. If the 2D $E_B(k_x,k_y)$ measurement, which provides such results as Fig. 5(e) as well as Fig. 6(a) and (d), is repeated at tens or hundreds different $h\nu$, a full 3D band dispersion $E_B(k_x,k_y,k_z)$ can in principle be obtained. In many cases, however, such a full 3D SX-ARPES with high resolution of energy and momenta requires too much measuring time. Although such measurements are still rather rare up to now, studies of 3D $E_B(k_x,k_y,k_z)$ must be the direction of ARPES to be intensively tackled from now on.

For ARPES studies clean surfaces of high quality single crystals are required. There are such possibilities as (1) in situ grown epitaxial single crystal surface, (2) clean surface prepared by ion-sputtering and annealing as well as (3) clean surface prepared by in situ cleavage. In the case of (1) and (2), one must pay attention to stoichiometry and homogeneity of the surface. In the case of (3), cleavage to realize a homogeneous surface is not difficult in the case of layered materials with two-dimensionality. In the case of single crystals with increased three-dimensionality, however, cleaved surfaces often show several or many tiny cleavage planes. If the spot size of the incident photon beam is larger than the small cleavage plane, the ARPES provides averaged information on several cleavage planes even containing undesired information on uncleaved regions. If the incident light is focused by mirrors or zone plate to a spot smaller than a single cleaved region, still reliable ARPES may be feasible [22]. In order to cover a wide (k_x,k_y) region, however, it is usually required to mechanically rotate the sample. In that case, it is rather difficult to fix the light spot within a small region on a small cleaved surface. Positioning of the high-quality cleaved region covering the photon beam spot in advance and during the measurement is required to overcome this difficulty [31,32].

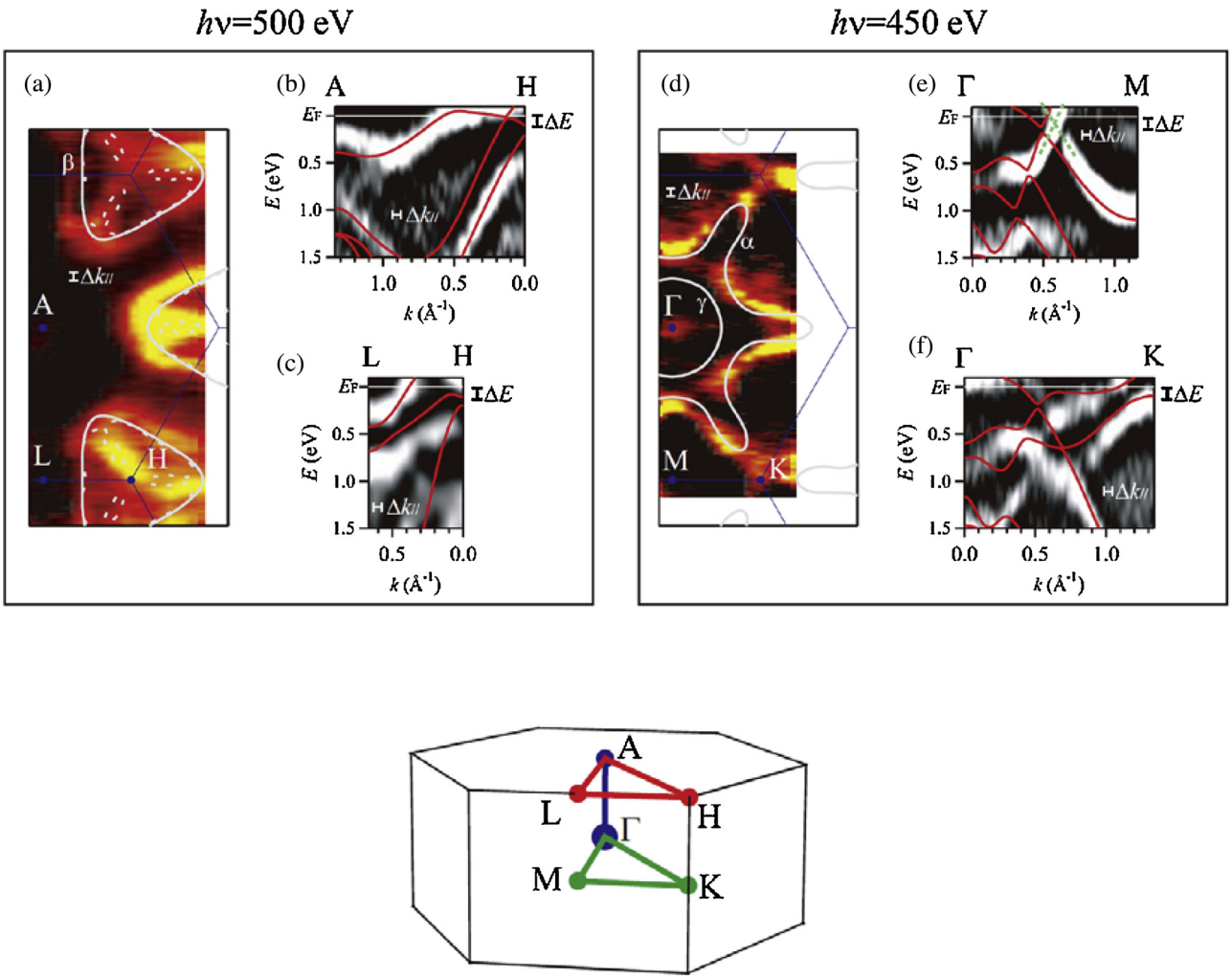

Fig. 6. FSs of UB_2 in the *A*–*H*–*L* and *Γ*–*K*–*M* planes derived from the ARPES at $h\nu$ = 500 and 450 eV with the energy resolution ~120 meV and $\Delta k_{||}$~0.06 Å^{-1}. Measurement is performed at 20 steps along the *Γ*–*K* $k_{||}$ values [30]. The inner potential V_0 is evaluated as ~12 eV.

4. Hard X-ray photoelectron spectroscopy

In order to realize increased bulk sensitivity, higher $h\nu$ photoelectron spectroscopy in the hard X-ray region (HAXPES) became very popular nowadays by use of planar undulator radiation. The advantage of HAXPES in the $h\nu$ region of ~4 to 8 keV is the much reduced surface spectral weight in the valence band region below a few percents in many cases, compared with SX-PES and SX-ARPES with few dozens of percents. On the other hand the disadvantage of HAXPES is the reduced photoionization cross section by several orders of magnitude of most orbitals with increasing $h\nu$. The behaviors of such orbitals as transition metal 3d, lanthanide 4f and oxygen 2p states, which play important roles in strongly correlated electron systems, are shown in Fig. 7 together with that of the transition metal 2p core state [33]. It is easily understood here that a very bright light source is required for the HAXPES studies of transition metal 3d and outer p orbitals of chalcogen atoms, which often have noticeable contribution in valence bands. This is the reason why a 25 m long planar undulator is developed and installed at BL19LXU of SPring-8 [34]. In addition, polarization of the light can be switched by employing a diamond phase retarder (wave plate) for hard X-rays to measure the dichroism in HAXPES [35].

The advantage of HAXPES is that the observed spectra are dominated by the bulk electronic structures owing to the long λ_{mp} beyond 100 Å. Surface degradation is not a serious problem in contrast to SX-PES and SX-ARPES. So bulk sensitive HAX-ARPES

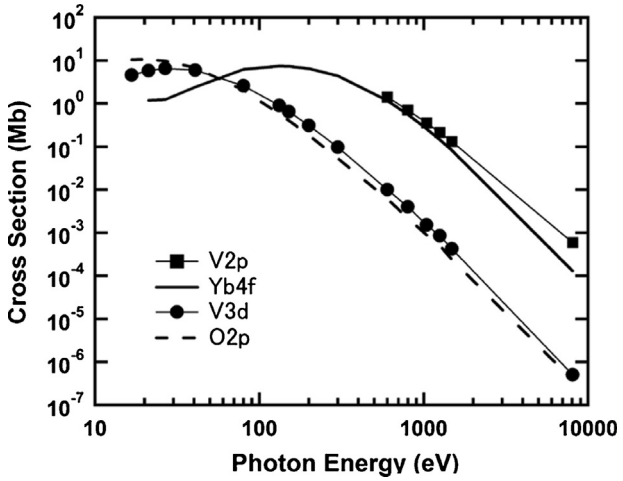

Fig. 7. Photon energy dependence of photoionoization cross sections of typical p, d and f orbitals [33].

is expected to provide useful information on bulk valence bands in various materials. However, there are two difficulties in HAX-ARPES. It is known that recoil effects on photoelectron emission take place not only in atoms and molecules but also in solids on photoemission of core levels of light elements [3]. The presence

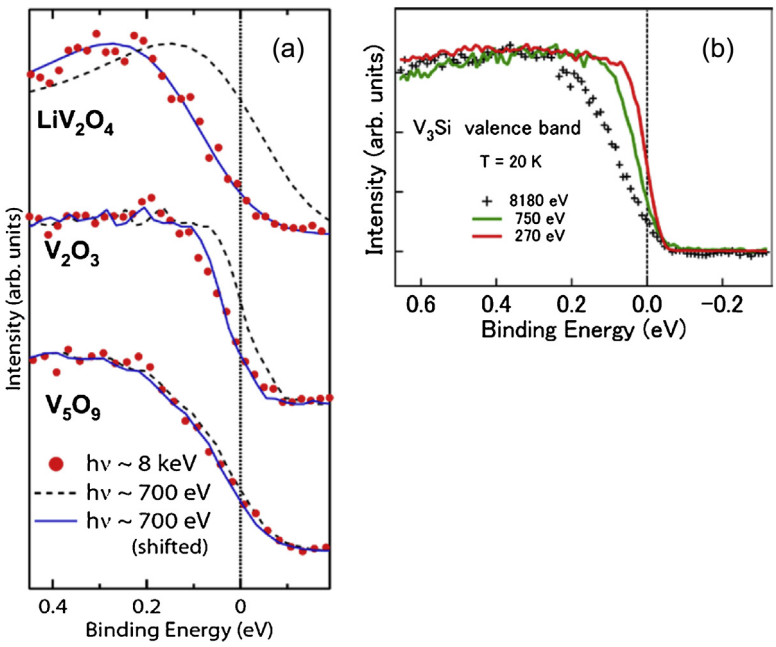

Fig. 8. Photoelectron recoil effects for the valence bands of some V compounds. LiV_2O_4 spectra at 20 K, metallic V_2O_3 at 175 K, metallic V_5O_9 at 150 K and V_3Si at 20 K [36–38]. The energy resolution was ~100 meV at $h\nu \sim 8$ keV and ~700 eV. It was set to ~50 meV at 270 eV.

or absence of the recoil effects is also found to depend on the individual materials even for the same core level [36,37]. The recoil effects are also observed for valence electron photoemission, though the wave function is not localized but extended over the crystal [3,36–38]. Depending on the individual orbitals and materials, the recoil behavior is diverse. Although a rigid-shift type recoil effect is observed for most core levels, the behavior is much different in the case of the valence band as seen in Fig. 8 for vanadium oxides and V_3Si. In the case of the valence band in V_3Si, the recoil shift depends strongly upon E_B. This kind of behavior can be understood as the relative spectral weight between V 3d and Si 3p changes with E_B. Namely, the relative weight of the partial density of states (PDOS) of Si 3p is understood to increase with E_B in this material. Since ARPES traces the peak energies of valence band structures as a function of (k_x,k_y,k_z), the revealed dispersions are strongly influenced by the different recoil shifts of the constituent electronic structures. Therefore careful attention is required for the bulk sensitive band mapping by HAX-ARPES.

Another difficulty of HAX-ARPES comes from the Debye–Waller factor, which is responsible for the wave vector (**k**) broadening due to the electron-phonon coupling in the photo-excitation process. When this factor W(T), which depends upon the temperature T, is large enough(>0.9 for example), the **k** broadening is not serious. If this factor is small (<0.1), however, the wave vector is broadened to a large extent [39]. HAX-ARPES results measured for W(1 1 0) at $h\nu = 5956$ eV and at 30 and 300 K reported in Ref. [39] are reproduced in Fig. 9. The room temperature ARPES results, corresponding to $W(T) = 0.09$ in Fig. 9(a) show modulated intensity distribution over wide k region. If projected to the E_B axis, good correspondence with density of states (DOS) is recognized. If projected to the k (or detector angle) axis, the dominant influence of the core-like X-ray photoelectron diffraction effect (XPD) is recognized as well. So it is difficult to obtain direct information on the band dispersive features in this case resulting from the low fraction of the direct photoemission process at room temperature. If measured at $T = 30$ K ($W(T) = 0.45$), phonon effects are suppressed and dispersive features are to some extent observed. If DOS and XPD effects are numerically removed, dispersive features of the valence bands are better revealed in reasonable correspondence with the results of model calculation. In order to compare the experimental HAX-ARPES results to theoretical prediction, one must additionally pay a deep attention to the orientation of the sample to the detector, since slight angle misalignment induces a serious deviation in the **k** space. So one must always keep in mind that the bulk sensitive HAX-ARPES is not straightforward applicable to bulk band mapping with high resolution.

5. Merit and limitation of very low energy photoelectron spectroscopy

Although modern SX- and HAX-PES and -ARPES are only feasible by use of high brightness synchrotron radiation beam lines with high stability, the beam time for measurement is usually rather tight due to the high demand of outside users and in-house staffs. Then low energy PES and ARPES by using rare gas lamps and laser light sources in small size laboratories are also becoming very popular nowadays in addition to the traditional use of He lamps. Advantage of the low $h\nu$ PES and ARPES is the feasibility of high energy resolution. In addition, possible easy switching capability of the light polarization facilitates the measurement of the dichroism in the angular distribution of photoelectron emission. In the case of lasers, tiny focusing of the light spot on the small sample or a small cleaved region on the sample further promotes the so called ELE(extremely low energy)-ARPES.

Generally speaking, λ_{mp} of the photoelectrons increases above 100 eV. However, the λ_{mp} below an electron energy of 10–20 eV depends strongly on the individual materials. If the electron energy is below the interband gap energy of insulators, λ_{mp} increases suddenly. Even in the cases of metals, it is often thought that λ_{mp} increases with decreasing electron energy as observed and/or predicted in many materials [40]. For instance, in the case of Fe_3O_4 with the Verwey transition at $T_V \sim 123$ K, the temperature dependence of ELEPES at $h\nu = 7.5$ eV is consistent with that of the HAXPES results at ~8 keV as shown in Fig. 10. This example demonstrates the bulk sensitivity of ELEPES in Fe_3O_4 [41]. A second example is $LiRh_2O_4$, which is a spinel type compound and shows a two-step metal-to-insulator transition at 230 K (from orbital-disorder to orbital-order metal phase) and at 170 K (to charge-ordered valence bond

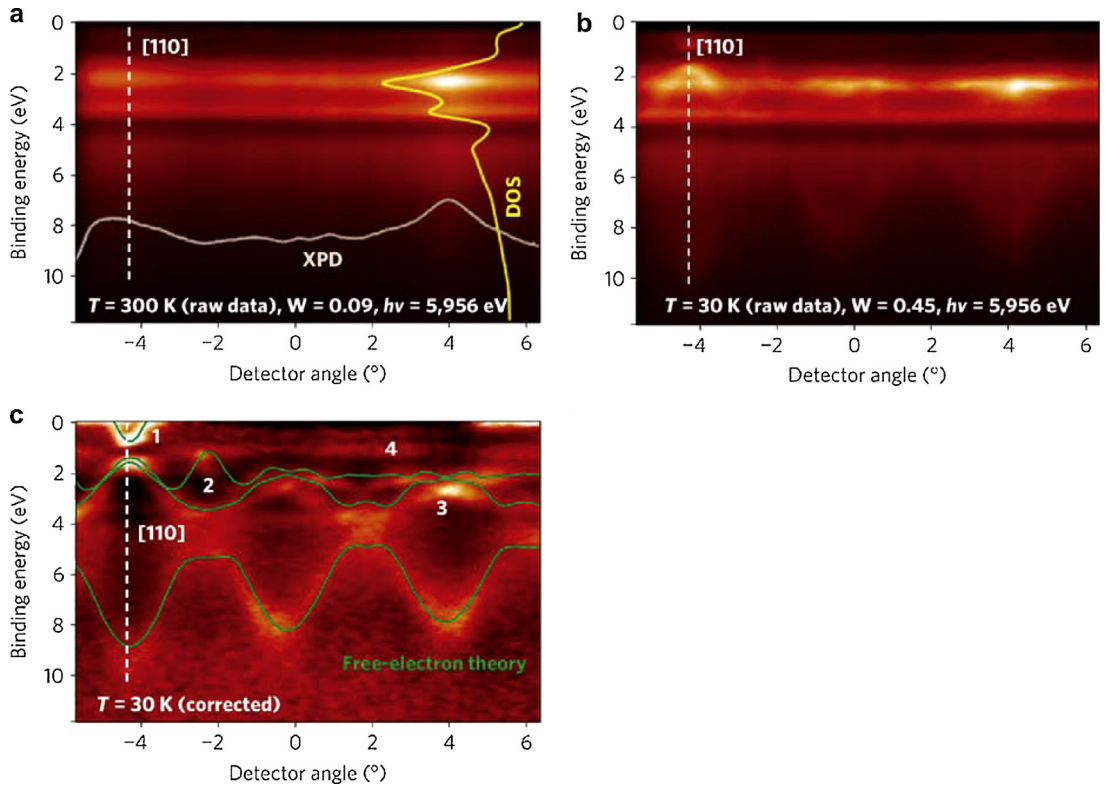

Fig. 9. HAX-ARPES of W(1 1 0) at $h\nu = 5956$ eV. Sample temperature is 300 K (a) and 30 K (b). The Debye–Waller factor is 0.09 at 300 K and 0.45 at 30 K. DOS effects and XPD effects are clearly seen in the spectra [39].

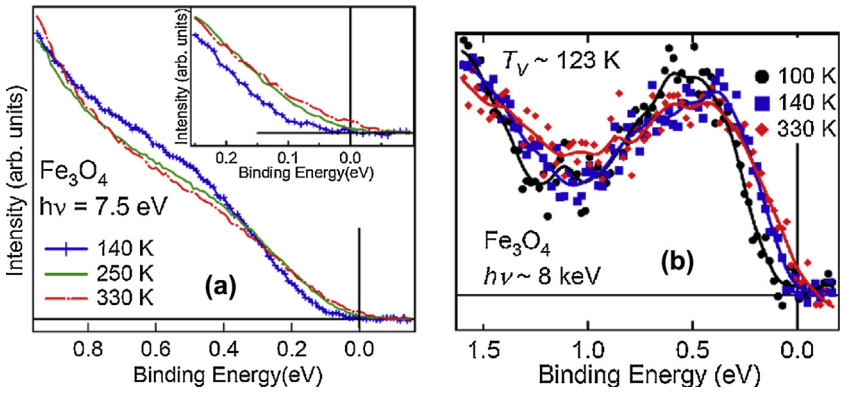

Fig. 10. Temperature dependence of the ELEPES at $h\nu = 7.5$ eV and HAXPES at $h\nu \sim 8$ keV of Fe_3O_4, which shows the Verwey transition at ~123 K [41].

insulator phase). Again, the ELEPES result at 8.4 eV is consistent with the HAXPES results at ~8 keV, showing the bulk sensitivity of ELEPES in $LiRh_2O_4$ [42].

In the case of $(V_{1-x}Cr_x)_2O_3$ system [43], however, less bulk sensitivity of ELEPES than HAXPES is experimentally confirmed [44] as shown in Fig. 11. In the paramagnetic metal phase (PM), the quasi-particle (QP) coherent peak near E_F is much stronger than the incoherent lower Hubbard band (LHB) in the bulk sensitive HAXPES (Fig. 11(c)) spectrum [44] as confirmed from the $h\nu$ dependent angle integrated spectra. In ELEPES spectra of a sample with $x = 0.011$ [43] measured in $\Delta k_{||} < 0.14\,\text{Å}^{-1}$ at $E_K = 5$ eV for the (1 0 2) cleaved surface in the PM phase, no pronounced QP was observed. On the (0 0 1) cleaved surface, however, a QP peak is observed by tuning $h\nu$ and k properly in a limited region as shown in Fig. 11(a). The emission angle (θ) dependence of the spectra at $h\nu = 9$ eV in Fig. 11(b) revealed that the intensity of the QP observed at $\theta = 0^\circ$ becomes much reduced for increased θ at 60°. The results in Fig. 11(b) suggest that the intensity of the QP peak is weaker than that of the LHB, if angle integrated ELEPS is derived from measurements at various θ. In comparison with the bulk sensitive angle integrated HAXPES in Fig. 11(c), the apparent surface sensitivity of ELEPES in the V_2O_3 system is confirmed.

Nowadays, spin-polarized Dirac cone states in the topological insulators [45] are attracting wide interest. It is demonstrated that ELE-ARPES is powerful to detect the surface Dirac cone state in these cases [46]. If no bulk state is accessible in the $E_B(k_x,k_y)$ region covered by the ELE-ARPES measurement and still some surface states are present, ELE-ARPES is an effective approach to perform the band mapping of such surface states [3].

In the ELE-ARPES, however, the region of E_K is rather limited depending upon the employed $h\nu$. Then chemical information is very difficult to be obtained in comparison with soft and hard X-ray photoelectron spectroscopy. The **k** region covered by the conventional ELE-ARPES measurement is also very limited. Higher $h\nu$

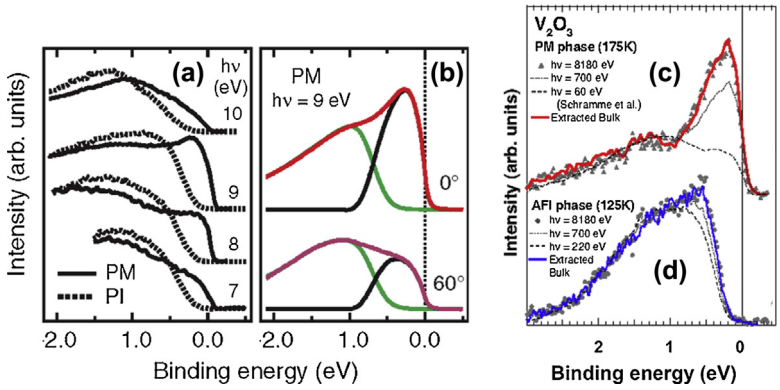

Fig. 11. (a) Normal emission photoelectron spectra of $(V_{0.989}Cr_{0.011})_2O_3$ measured on the (0 0 1) surface at 300 K (PI) and 200 K (PM) for $h\nu$ = 10, 9, 8 and 7 eV. (b) Spectra of V_2O_3 on the (0 0 1) surface at $\theta = 0^\circ$ and 60° are shown by the top(red) curves, which are separated into the quasi-particle peak at smaller E_B(black) and the lower Hubbard band peak at larger E_B(green) [43]. Bulk spectra of V_2O_3 in the PM and AFI phases are shown in (c) and (d) [44].

ARPES enables one to cover wider regions of E_B and **k**. A wide **k** region can be covered even at low $h\nu$, however, by use of a momentum microscope as explained later in Section 7.

6. Spin polarized photoelectron spectroscopy: Past and present status

The detection of the electron spin has been a major issue in photoelectron spectroscopy. The reason is that an "ideal" spin filter for free electrons, like in a Stern–Gerlach type experiment for atoms, cannot be realized due to the Heisenberg uncertainty relation. The spin detection of photoelectrons is therefore typically done in a scattering experiments exploiting the spin dependency of Mott-scattering, or spin-polarized low energy electron diffraction (SP-LEED), both based on the spin-orbit coupling in the target material.

Information on the spin polarization of photoelectrons is very demanded in order to understand the electronic structure of solids such as topological insulators and exotic superconductors. Although studies of the electronic structure under an external magnetic field are possible by photon spectroscopy, angle resolved photoelectron spectroscopy is usually not feasible since the trajectory of the photoelectron is strongly influenced by the Lorentz force in the magnetic field. Therefore the spectroscopy of spin-polarized electrons is usually performed without an external magnetic field. The photoelectrons excited by circularly polarized light are often spin-polarized due to the spin-orbit coupling and selection rules. In the case of ferro- and ferri-magnetic materials, the spin resolved ARPES (SP-ARPES) is still possible on remanently magnetized sample if the residual magnetic field is not too strong.

The spin polarization of the photoelectrons is defined as $P_s = (n\uparrow - n\downarrow)/(n\uparrow + n\downarrow)$, where $n\uparrow$ and $n\downarrow$ stands for the electron numbers with opposite spins. Various spin detectors have so far been developed and employed in SP-PES and SP-ARPES. The Mott detector was most widely employed in the past [4] and still producing new results. Its working principle can be understood from the following Dirac equation:

$$\left[\frac{(\mathbf{p}+e\mathbf{A})^2}{2m} - e\Phi + e\hbar\sigma\cdot\frac{\mathbf{B}}{2\mathrm{m}} - \frac{ie\hbar\mathbf{E}\cdot\mathbf{p}}{4m^2c^2} + \frac{e\hbar\sigma\cdot(\mathbf{E}\times\mathbf{p})}{4m^2c^2}\right]\psi = W\psi,$$

where $W + mc^2$ is the total energy, **p** is the electron momentum and **A** is the vector potential. Φ, σ, **B** and **E** are the scalar potential, electron spin, magnetic and electric fields. The last term on the left hand side stands for the spin-orbit interaction energy, which induces the left(L)–right(R) scattering asymmetry of the electrons incident onto the target (often Au thin foil but other heavy elements as well). The experimentally evaluated asymmetry as $A(\theta) = (N_L - N_R)/(N_L + N_R)$ can be used to estimate the spin polarization P_s of the photoelectron by $P_s = A(\theta)/S(\theta)$, where $S(\theta)$ is the Sherman function, i.e., the spin sensitivity of the detector. $S(\theta)$ depends upon the target material, electron collision energy and the range of θ and can be evaluated experimentally. The effective Sherman function S_{eff} of Mott type polarimeter lies in the range of 0.1–0.4. Then the figure of merit f_0 defined as $(I/I_0)S_{\mathrm{eff}}{}^2$, where I_0 is the electron current entering the polarimeter and I is the total scattered current detected by the left and right detectors, lies in the range up to 2×10^{-4}. In the case of a 25 kV compact mini-Mott spin polarimeter, $S_{\mathrm{eff}} = 0.17$ and $f_0 = 1.4 \times 10^{-4}$ were reported [47]. In the case of the Mott detector, only single channel spin detection was possible, though the $P_{s||x}$ and $P_{s||y}$ components (x and y lie in the target surface plane) could be simultaneously measured.

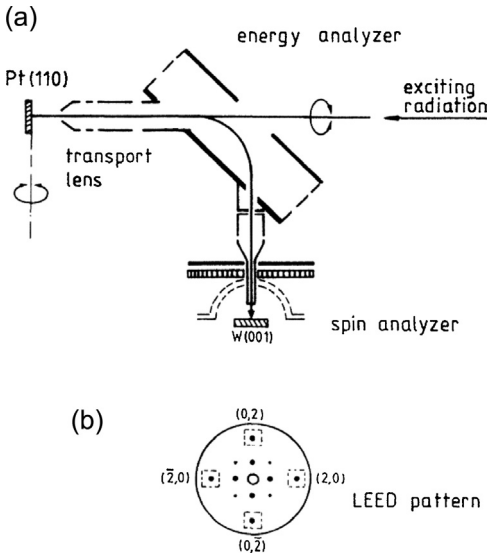

Fig. 12. SP-ARPES set up employed to measure the photoemission spectra of Pt(1 1 0) [50]. W SP-LEED detector is used after the electron energy analysis by a cylindrical mirror analyzer. Four LEED spots, (0,2), (2,0), (0,−2) and (−2,0), are used to evaluate the two spin components [6].

The low-energy-electron-diffraction (LEED) spin detector based on a W single crystal (W SP-LEED detector) was later developed [6] and used for SP-ARPES. As schematically shown in Fig. 12(a) and (b), the electrons passed through the central hole of a

resistive-anode and MCP (micro channel plate) hit the W(0 0 1) surface at 104.5 eV kinetic energy in the normal incidence configuration. The four (2,0) LEED spots are simultaneously detected providing information on $P_{s||x}$ and $P_{s||y}$ components parallel to the W(0 0 1) surface. The small size of this detector due to the use of a much lower electron energy compared to the 100 kV or 25 kV Mott detector is a primary advantage [48]. $S_{\text{eff}} = 0.27$ and $f_0 = 1.6 \times 10^{-4}$ were realized and applied to SP-ARPES [49,50] and core level SP-PES [51]. In the case of W(0 0 1) detector, however, surface cleaning by flashing is frequently required (every 0.5 to 2 h) in a vacuum better than 1×10^{-8} Pa [52,53].

As we see from these examples, the low efficiency of widely used spin detectors is on one side based on the scattering process, which can be improved by spin-detector target materials which have a higher spin asymmetry and higher reflectivity. On the other side, conventional spin detectors can only measure one spin-resolved data point ("channel") at a time. Extended data sets, like energy spectra or angular scans, have to be measured sequentially point by point. Such a requirement is especially a problem for spin detection experiments where only low intensities are available. For instance this is the case for high-resolution ARPES measurements, in which the single-channel spin detection requires sequential scanning of a certain wave-vector and energy interval. HAXPES measurements are another case where count rates are very low due to a combination of low photoionization cross-sections at hard X-ray energies and limited angular acceptance of electron spectrometers. In these cases, experiments on reactive samples are prevented because only a short time period for measurements is available against surface deterioration.

In practice, spin-resolved spectroscopy with sufficient count rates can often only be performed with strongly reduced energy and angular resolution. In the case of spin-integrated electron spectroscopy, however, the situation is completely different: With the advent of multi-channel detection, the efficiency of electron spectrometers increased dramatically. Today, state-of-the-art electron energy analyzers feature highly efficient multi-channel detection with more than 10^4 data points acquired simultaneously as will be further discussed in Section 7.

One of the recent and noteworthy development is the Fe(0 0 1)-$p(1 \times 1)$—O VLEED spin detector [54,55] (VLEED: very-low-energy-electron-diffraction). Spin exchange interaction is used to measure the spin polarization of the electrons incident onto the magnetized ferromagnetic target as illustrated in Fig. 13 [56], where the angle of θ_{in} for specular (or mirror) reflection was set to ~6.5° ($2\theta_{\text{in}} = 13°$). In contrast to the left-right scattering intensity asymmetry in the case of Mott and W SP-LEED detectors, spin information is derived from two successive measurements with reversed target magnetization [54–57]. In the case of Fig. 13, spin polarization along the x and z, namely P_x and P_z can be obtained, for example, by changing the magnetization direction of the Fe(0 0 1)-$p(1 \times 1)$—O detector by 90°. In contrast to the original design of Fe deposition onto a Ag(0 0 1) surface [58], the oxygen passivated Fe(0 0 1)-$p(1 \times 1)$—O surface, grown on a MgO(0 0 1) or W(0 0 1) substrate, could prolong the effective lifetime of the Fe(0 0 1) target to few months. By tuning the electron incidence energy onto the target properly, a large spin asymmetry was realized for the specularly reflected electrons. $S_{\text{eff}} \sim 0.40$ and $f_0 \sim 1.9 \times 10^{-2}$ were obtained for $E_K = 6$ eV. Then very efficient SP-ARPES became feasible as in Fig. 14 [56] even in the single-channel detection. The f_0 of this spin detector is almost two orders of magnitude higher than those of preceding spin detectors and its nice performance can be kept for a long time. According to spin-dependent low-energy electron reflection measurements over a wide range of incident electron energies from 2 eV up to 17 eV and θ_{in} from 25 to 76°, detailed behaviors of S_{eff} (θ) and f_0 were clarified [57]. The f_0s derived for the collinear configuration between the photoelectron spin

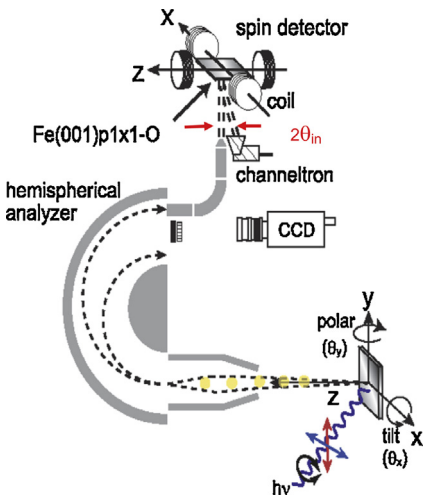

Fig. 13. Single-channel SP-ARPES instrument based on the Fe(0 0 1)-$p(1 \times 1)$—O VLEED spin detector after the hemispherical electron energy analyzer (HDA) [54,56]. Energy and angle resolved electrons are incident onto the spin detector with the incidence angle θ_{in} from the surface normal and specularly reflected electrons are detected. The spin asymmetry is evaluated from two measurements performed by reversing the magnetization direction of the Fe(0 0 1)—O detector. The spin polarization along the x and z directions can be evaluated by this instrument. (k_x,k_y) region of the sample is selected by rotating the sample.

polarization **P** and the target magnetization **M** (either ↑ or ↓) are shown in Fig. 15. A maximum f_0 of more than 2×10^{-2} for $\theta_{\text{in}} = 45°$ is found at $E_K = 3$ eV. At $E_K = 2.8$ eV and $\theta_{\text{in}} = 45°$, even higher $f_0 = 2.8 \times 10^{-2}$ was obtained. Since the E_K to be used for spin detection in this case is rather low, very careful reduction of the residual magnetic and electric field is required for evaluation of the spin polarization of photoelectrons.

In many cases of SP-ARPES, full 3D spin vectorial analysis is indispensable [59], for example, in the case of the out-of-plane spin component in topological surface states [60]. Three orthogonal spin components can be measured by two VLEED spin detectors if the second VLEED detector is located on the orthogonally deflected electron orbit from that for the first VLEED detector [59].

In order to dramatically improve the detection efficiency, multichannel $k_{x,y}$ resolved spin detection is desirable as discussed in Sections 7 and 8.

7. Momentum microscopy

7.1. The principle and advantage of momentum imaging

As outlined above (Section 3, Fig. 3) modern conventional hemispherical deflection electron energy analyzers (HDAs) used today in ARPES experiments employ a two-dimensional detection scheme. An imaging detector is placed in the exit plane of the analyzer, which allows to record the emission angle (θ) and the binding energy (E_B) at the same time, within a limited interval. The measurement of larger intervals or of the second in-plane emission direction requires scanning of the analyzer or sample position. Due to the second order aberration inherent to the HDA [61], the ultimate resolution can only be achieved by the restriction to small slits and small photon beams, at the cost of measurement speed.

A different approach for the simultaneous measurement of a 2D distribution of photoelectrons was to make use of the imaging properties of a photoelectron emission microscope (PEEM). In a PEEM, photoelectrons from the sample are collected by the objective lens. This lens immerses the sample in a strong electric field of a few kV/mm. This is why this objective lens, which forms the first optical element of the PEEM, is often called "immersion lens", or "cathode lens" to point out that the sample, i.e., the cathode, is

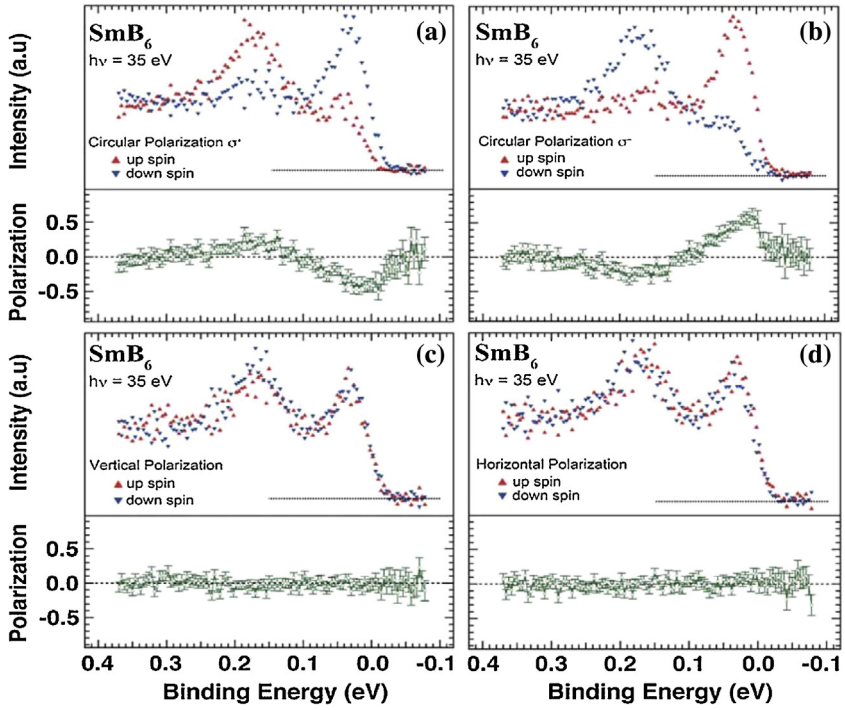

Fig. 14. SP-ARPES of Kondo insulator SmB_6 measured at 35 eV and 12 K [56]. σ^+, σ^-, linearly polarized light excitations for the spectra (a), (b), (c), and (d). The intensity is given in an arbitrary unit (a.u). The spin parallel to the *x*-axis in Fig. 13 is observed for the circularly polarized light excitation. Spin polarization is, however, not observed for the linearly polarized light excitation on this surface.

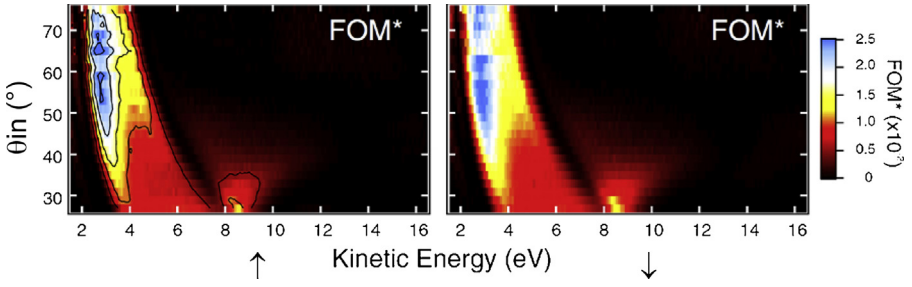

Fig. 15. Figure of merit f_0 of Fe(0 0 1)-$p(1 \times 1)$—O VLEED spin detector as a function of θ_{in}(angle of incidence of electrons) and incident electron energy [57]. ↑ and ↓ correspond to two opposite magnetization directions of the passivated Fe target. Photoelectron spin polarization **P** and target magnetization **M** lie in the scattering plane in order to exclude the spin-orbit effects. Five lines in the left panel correspond to $f_0 = (2.5, 2.0, 1.5, 1.0 \text{ and } 0.5) \times 10^{-2}$.

part of the electron optical system. Fig. 16 illustrates the effect of the accelerating field. Electrons that are emitted from the sample surface are accelerated along the sample normal. Therefore, even those photoelectrons that were emitted at angles up to $\theta = 90^\circ$, i.e., parallel to the surface, enter the lens under a finite angle θ', and the lens sees a virtual image of the sample that is located behind the real sample surface. Here θ' and θ satisfy the following equation [62]:

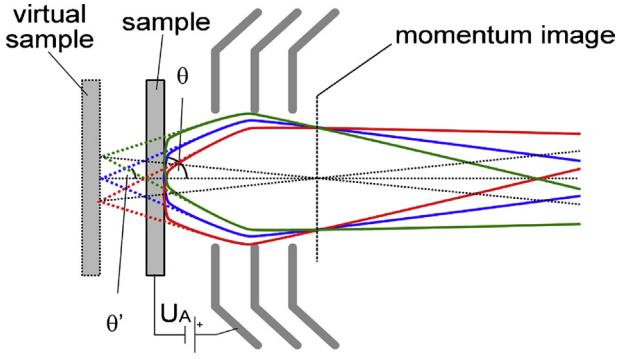

Fig. 16. Effect of the immersion field between the sample and the microscope lens. The microscope sees a virtual sample with an effective finite emission angel θ'. The momentum image is formed in the focal plane (vertical dotted line) with linear (k_x, k_y) scale.

$$\sin\theta = \sin\theta' \sqrt{\frac{eU_A}{E_0} + 1} \tag{7.1}$$

The momentum coordinate parallel to the surface, $k_{||}$, is preserved during this acceleration due to the cylinder symmetry. When the acceleration voltage, U_A, is large compared to the kinetic energy, E_0, of the photoelectrons, $U_A \gg E_0$, Eq. (7.1) is simplified to

$$\sin\theta' \propto k_{||} \tag{7.2}$$

and the image formed in the momentum focal plane (plane shown by the vertical dotted line) of the PEEM objective lens is scaled linear in $k_{||}$ [8,62].

In a PEEM experiment, the magnified real space image of the sample, formed further downstream in Fig. 16 will be projected onto a 2D detector. In the momentum microscope, which is described in detail later in Section 7.2 and Fig. 20, the momentum image will be projected onto this 2D image detector. The typical

detector is a combination of MCP and fluorescent screen, read out by a CCD camera. However, other types of detectors might be used, such as time-resolving delay line detectors [63], or direct electron semiconductor detectors which may provide improved signal to noise ratio and dynamic range [64]. As the momentum component parallel to the surface is preserved in the photoemission process, this momentum image directly represents a cut through the band structure of the sample with respect to the crystal momentum k_x and k_y at a certain energy. In contrast to a conventional ARPES experiment, no conversion from emission angles (θ) to crystal momentum (**k**) is necessary, and all electrons that are emitted from the sample into the complete half-space are collected.

We note that the sample is always kept at a fixed angle with respect to the optical axis of the momentum microscope, unlike in conventional ARPES setups where the angle is scanned during the measurement. As typical instruments use an acceleration voltage of several kV up to several 10 kV, the collection of photoelectrons within the complete solid angle above the surface is possible even at excitation energies of $h\nu \geq 100$ eV, and the momentum images cover more than the first surface BZ of typical materials.

In an early demonstration of momentum microscopy, the kinetic energy of the photoelectron was fixed to the high energy cutoff of the spectrum at the Fermi edge, using a retarding field analyzer [62]. This limited the practical use to the measurement of constant energy cuts through the Fermi surface of a solid. This is in particular useful, when combined with an excitation light source with a variable photon energy $h\nu$, like synchrotron radiation. The efficient detection of 2D $E_F(k_x, k_y)$ cuts through the Fermi surface allows recording of large data sets with different $h\nu$, in a more efficient way than introduced in Section 3, above. As shown in Fig. 17, measurements over a range of $h\nu$ allow one to scan through the perpendicular momentum component $k_\perp$, which is selected by momentum conservation under the assumption of a free-electron final state for the photo-excitation [3,62]. Such a 3D data set $E_F(k_x,k_y,k_z)$ provides a tomographic view of the Fermi surface of the sample.

Later, Krömker et al. presented a more versatile momentum microscope [65]. As before, this instrument combines a typical PEEM column as used in Ref. [62] with an imaging energy filter based on two HDAs arranged in an S-like geometry to compensate the second order aberration of conventional analyzers [66]. This combination enables the fast acquisition of the three-dimensional (E_B, k_x, k_y) maps of the band dispersion. In particular, the data beyond high-symmetry directions provides valuable input for quantitative theoretical models.

As an example, Fig. 18(a) shows a measurement of a Cu(1 1 1) surface. This particular momentum image shows the photoemission intensities of the *d*-electron states at 2.35 eV below the Fermi energy [67]. As the measurement of each 2D momentum image only takes a couple of minutes, using a He discharge light source, a whole series of such images can be easily acquired, containing the information of the $E_B(k_x,k_y)$ band dispersion in all directions of the surface BZ (see Fig. 18(d)). The 2D (k_x,k_y) momentum images display true intensities of the photoelectron current in all directions, without the symmetrization typically applied in conventional angle scanned ARPES maps. For instance, we can observe an unequal brightness of the bands on the left and right side of the image, while the presence and shape of the features follows the three-fold symmetry of Cu(1 1 1). This effect, known as the linear dichroism in angular dependence (LDAD) [68], is caused by the off-normal incidence of the light onto the surface, breaking the three-fold symmetry.

The comprehensive data sets allow a direct quantitative comparison with advanced theoretical models. Such an example is displayed in Fig. 18(b) and (e), where the photoemission intensities were calculated within the one-step model for the same geometry

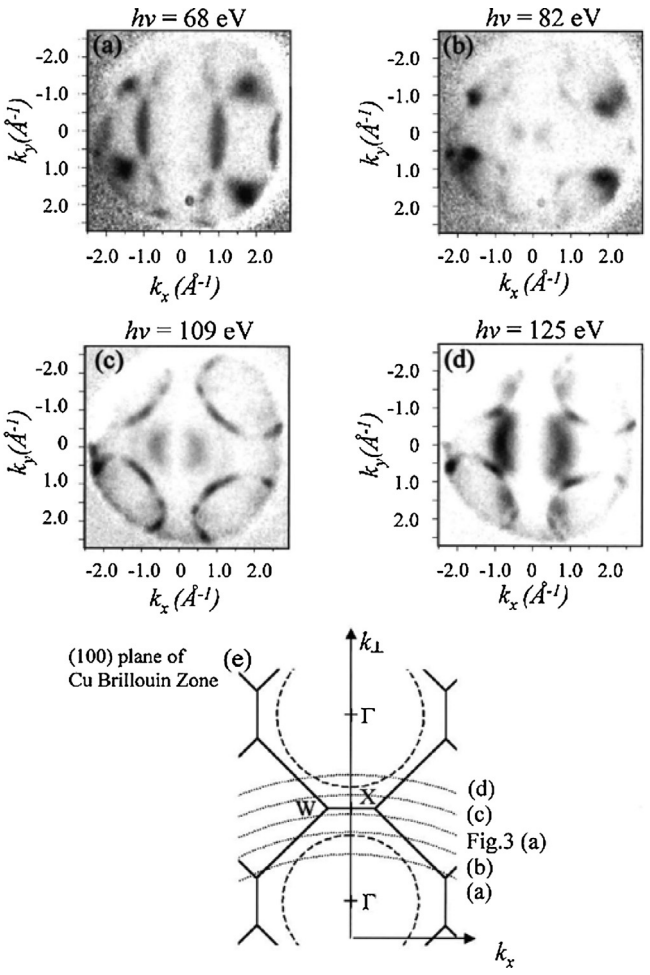

Fig. 17. (a)–(d) Two dimensional cuts through the Fermi surface of copper measured at different photon energies [62]. (e) Region of the bulk copper Brillouin zone along the $k_\perp$ direction sampled by (a)–(d).

as in the experiment. The two-dimensional intensity patterns are particularly sensitive to the relative energetic position of different bands that intersect the image. In the case of copper, states with sp- and d-symmetry are present, and it was demonstrated that a remarkable agreement between the theory and the measured intensities is obtained by taking into account the electronic self-energy, Σ, through an orbital dependent renormalization [69] of the LDA potentials by $\Sigma_d = -0.8$ eV for the d-states and by $\Sigma_{sp} = +0.3$ eV for the sp-states. While this works well for a weakly correlated material like copper, we note that the electronic self-energy is a non-local operator that depends on energy, wave vector, layer, and orbital momentum. Given the complete experimental mapping of the valence electronic structure, a detailed comparison with theoretical photoemission patterns will provide a crucial test for many-body corrections, especially for systems with strong electron correlations.

7.2. Present status of momentum microscopy instrumentation

The previous examples showed that the measurement principle of the momentum microscope to record $E_B(k_x,k_y)$ maps in a single image has many advantages over the measurement principle of conventional angle scanning ARPES. The wide acceptance angle of photoelectrons of ±90° gives access to the complete surface BZ, even when laboratory light sources with a limited $h\nu$ are used. In particular with laser excited photoemission, measurements cover

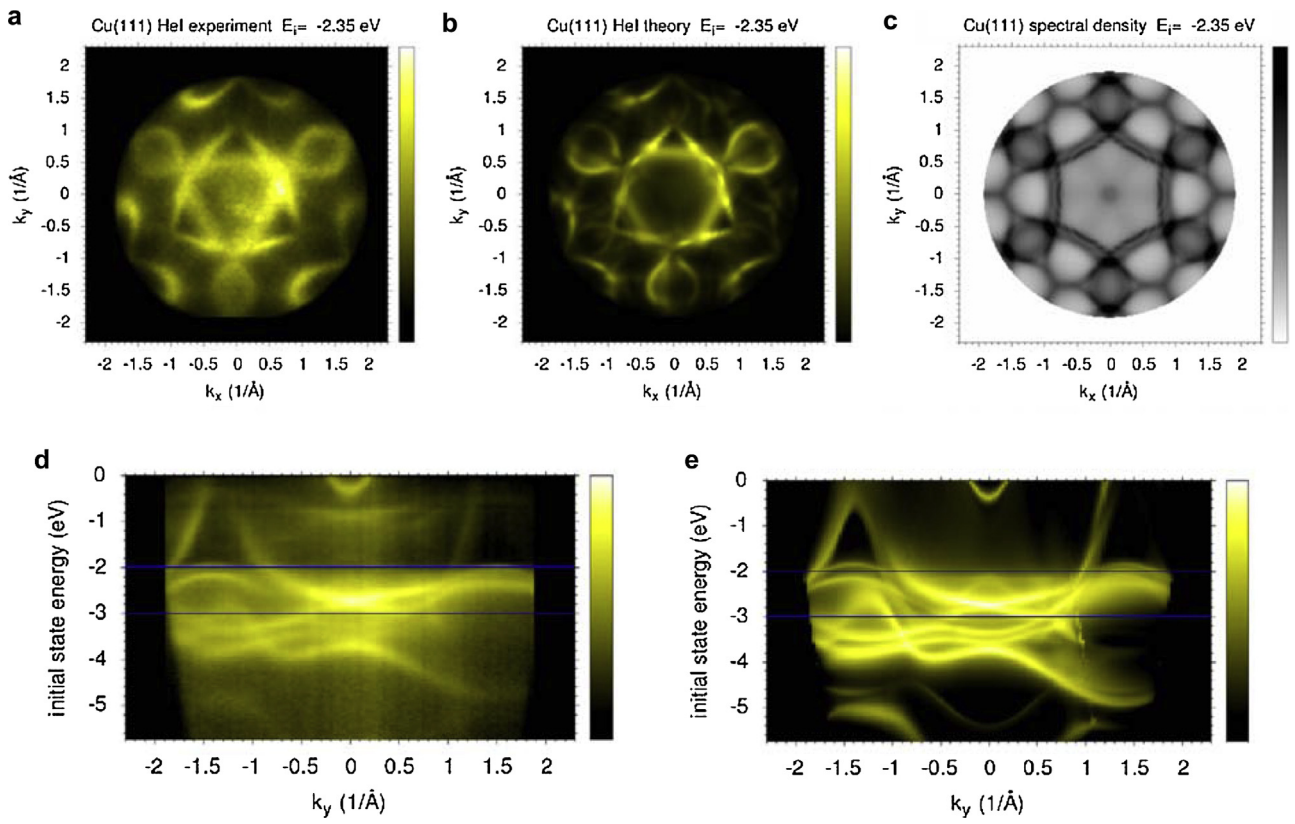

Fig. 18. (a) Experimental photoemission map of the d-states of Cu(1 1 1) [67], excited by He-I radiation from a laboratory light source. (b) One-step photoemission calculation including orbital dependent corrections for the electronic self-energy of $\Sigma_d = -0.8$ eV for the d-states and $\Sigma_{sp} = +0.3$ eV for the sp-states. (c) Spectral density calculated with self energy like in (b). (d) Band dispersions along the k_y direction from the experiment, and (e) from the theory.

a $k_{||}$ range that is more than three times larger compared to conventional ARPES spectrometers which have a limited angular acceptance of typical ±15°. As a practical example, using 6 eV photons the maximum kinetic energy of photoelectrons from E_F is ~1.5 eV (with work function 4.5 eV), and the maximum $k_{||}$ of an electron emitted parallel to the surface is ±0.63 Å^{-1}. This corresponds to the radius of the (k_x,k_y) image, and is enough to access half of the surface BZ of most materials. With a fixed collection angle interval of ±15°, however, the momentum range is only ±0.16 Å^{-1}, which fundamentally limits the uses of low $h\nu$ in conventional ARPES. The fixed photoemission geometry, where the angle of incidence of the photon beam stays constant with respect to the crystallographic axes of the sample, gives direct access to photoemission selection rules depending on the symmetry of wave functions and light polarization [70]. In addition, as momentum microscopy is based on the principles of PEEM, the analysis of microscopic sample areas is inherent to this technique.

This is particularly useful for the investigation of spatially inhomogeneous samples as mentioned before in Section 3, where the analyzed area might be selected by PEEM. Fig. 19(a) shows a few monolayers thick graphene grown on a SiC substrate. The coverage is not homogeneous, but the spectroscopic PEEM measurement reveals different areas with different work functions and coverage from 1 ML to 3 ML, with few 10 μm in size [71]. In Fig. 19(b), one region that was identified as 2 ML coverage was selected to record the band dispersion, revealing the Dirac cone states of the graphene [71]. It is important to note that the Dirac cone states of graphene are located at the K and K' points of the Brillouin zone. Features like the secondary Dirac cones, rotated by 21.9°, might be easily missed in conventional ARPES experiments. Compared to micro-spot ARPES [21,31,32] setups using synchrotron radiation, momentum microscopy has the great advantage that no

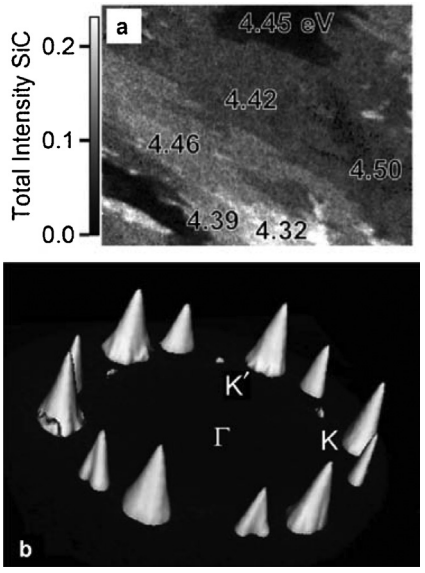

Fig. 19. (a) PEEM intensity map (field of view 53 μm) of the C1s substrate peak of multilayer graphene on SiC [71]. Numbers indicate the work function of different areas with 1 ML to 3 ML coverage. (b) 3D representation of photoemission data collected from the 2 ML (4.42 eV) region of (a). The Dirac cones of graphene at the K and K' points of the Brillouin zone are clearly visible. In addition, secondary Dirac cones rotated by 21.9° are observed.

scanning of the sample angle is required that might change the analyzed area in dependence of θ due to improper alignment [31]. By today, momentum microscopy systems of the first generation are also combined with synchrotron sources [71,72], enabling a

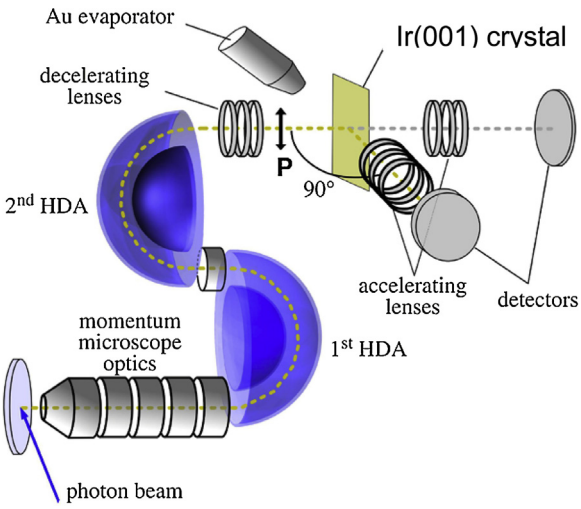

Fig. 20. Outline of the momentum microscope system with imaging spin filter, consisting of He-cooled sample stage, imaging electron optics, two HDAs, and detection branches for spin-integral and spin-filtered imaging. The Ir(0 0 1) crystal can be inserted/retracted after the 2nd HDA [8].

combination of core-level XPS imaging and spatially resolved band-structure measurements in the VUV to soft X-ray regime.

The early attempts of momentum microscopy systems paid these advantages by a rather coarse resolution of about 150 meV in energy [72] and 0.03 Å^{-1} in the $k_{||}$ momentum coordinate [65]. For many of today's applications for ARPES, these resolutions are not suitable. However, recent advances of momentum microscope instruments have shown that the limitations of early instruments are not a fundamental issue of the principle of momentum microscopy. Instead, optimization of the electron optical system beyond the previous simple modification of PEEM towards the requirements of momentum microscopy leads to a dedicated instrument that supersedes the conventional ARPES spectrometers in terms of resolution and accuracy in the $k_{||}$ maps. With a recently developed momentum microscope of this advanced generation, a $k_{||}$ momentum resolution $<5 \times 10^{-3}$ Å^{-1} and energy resolution of 12 meV are obtained [8], even when a conventional gas-discharge light source is used. This $k_{||}$ resolution corresponds to an angular resolution of $\Delta\theta = 0.1^\circ$ assuming He-I illumination, realized by the state of the art of current ARPES setups. We note and stress, however, that the $k_{||}$ imaging introduced in Eq. (7.2) has the consequence that the $\Delta k_{||}$ resolution of the instrument stays constant when increasing the $h\nu$, e.g., to the soft and hard X-ray range. This is not the case with conventional angle resolving spectrometers where the wave vector resolution becomes worse at high $h\nu$ due to their limited $\Delta\theta$.

Fig. 20 shows the schematic setup of a momentum microscopy system used for spin resolved measurements. As discussed above, a strong electric field is applied between the sample and the first electrode of the momentum microscope optics (objective lens or immersion lens) that collects the photoelectrons. In this particular example, a positive voltage of 20–30 kV is applied to this electrode. Here, the sample is kept near ground potential which allows an efficient cooling by liquid helium, such that sample temperatures below 20 K could be reached during the measurement [8]. We note that the fixed emission geometry further simplifies the design of the cryogenic sample stage, as no mechanical scanning is required. After the objective lens, the momentum microscope optics has a column of additional electron optical lens elements that are used to project the momentum image onto the final imaging electron detector, passing through an imaging energy filter composed of two HDAs in an S-like arrangement. In Section 3, we discussed the measurement of 2D images in conventional ARPES analyzers, where one image coordinate corresponds to the energy axis. For momentum microscopy, the HDA is operated in a different way as we need monochromatic images, i.e., the transmitted electron energy is (nearly) constant at all image points, while both image coordinates correspond to the respective in-plane momentum. Namely, all photoelectrons, sorted with respect to their (k_x,k_y), enter the imaging energy filter. Then at the output of this filter, the image $E_B(k_x,k_y)$ at the selected binding energy E_B is obtained and recorded by the detector.

Energy filters with this S-like arrangement of HDAs have been used before in the first attempt of a momentum microscope [65]. Electrons that pass the entrance plane of the first HDA analyzer are deflected in the spherically symmetric $1/r$ potential (r being the radius), and like in Fig. 3, have the largest energy dispersion after 180°. There, the image is energy dispersed and subject to the second order aberration that limits the usable transmission of conventional spectrometers [61]. By coupling the trajectories to the entrance of the second HDA, an effective 360° path is realized. As described earlier [66,73], the solution for this 360° deflection is a well known problem in classical mechanics and leads to closed trajectories (Kepler ellipses). Consequently aberrations are compensated at the output of the tandem HDAs energy filter arrangement, while the constant energy is selected by a small aperture in the symmetry plane. The resolution of this type of analyzer is in general not limited by the aberrations of conventional spectrometers, increasing the transmission and the measurement efficiency of the momentum microscope. With two HDAs with a mean radius of 150 mm and 200 μm wide energy defining slits, a resolution of 12 meV was measured at the Fermi edge on an Au(1 1 1) surface [8].

Beside this aberration compensated energy filter consisting of two HDAs in an S-like arrangement, other types of imaging energy filters can be used for momentum microscopy, as well. The most simple energy filter which was used to demonstrate the principle of momentum microscopy is based on a retarding field analyzer [62]. Related to the field penetration at the retarding grid arrangement, the energy resolution of this energy filter in the order of 500 meV is rather coarse. It was shown, later, that an improved design can reach a resolution of about 70 meV [74]. However, a fundamental limitation of this type of retarding field imaging energy filter is that the measurement is limited to the Fermi energy, which makes it unsuitable for general band structure measurements. In spectroscopic low energy electron microscopy (LEEM) and PEEM also other imaging energy filters based on a single HDA [75] were integrated in the column of the microscope, also enabling the acquisition of momentum images [76]. In LEEM instruments, the dispersion of the magnetostatic beam separator can also be used as an energy filter, when proper small slits are introduced in the dispersion plane [77]. Energy filtering is accomplished at a high kinetic energy of the electrons, in this case. Therefore good energy resolution requires narrow analyzer slits. Energy resolutions of 300 meV and 150 meV were reported in Refs. [76,77], respectively.

It is commonly believed that an advantage of conventional 2D ARPES analyzers is the ability to record one (E, $\theta_{||}$) image representing the band dispersions $E_B(k_{||})$ that one is usually interested in. Using a momentum microscope, on the other hand, a series of $E_B(k_x, k_y)$ images are needed to get the full band dispersion. Then one might think that it is more efficient to use a conventional spectrometer, at least when the respective bands live in a small energy- and momentum-window. For replying to this question, a particular example is shown for the surface state of Au(1 1 1) that exhibits a Rashba-type spin-splitting due to spin-orbit coupling [78,79]. In Fig. 21(a), we show a measurement of the Fermi surface contour of the surface state, observed as two concentric rings with opposite in-plane spin orientation. The measurement was conducted with the setup of the momentum microscope described above with the

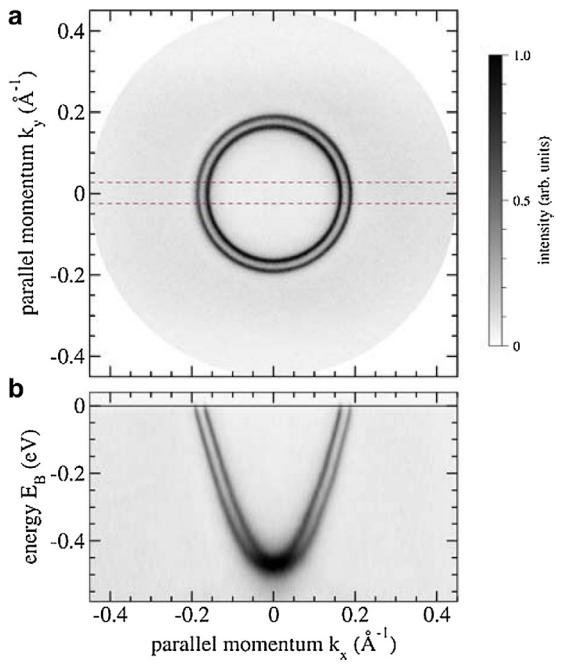

Fig. 21. (a) Momentum image of the Fermi surface contour of the Rashba-split surface state on Au(1 1 1) measured at $T = 18$ K and illumination by He–I radiation, (b) dispersion of the surface state obtained by a horizontal ($k_y = 0 \pm 0.025$ Å^{-1}) cut through the 3D data set as indicated in (a).

energy resolution set to 12 meV and an instrumental $k_{||}$ resolution of 0.005 Å^{-1}. The measurements of the FS contour using the He-I line of a gas discharge lamp took a total time of 15 min.

In order to obtain the dispersion of the surface state with the same counting statistics, we record a series of these images at different E_B. We note that each 2D momentum map, $E_B(k_x,k_y)$ has a resolution of $\Delta k_{||} = 0.005$ Å^{-1} in the k_x and k_y direction. This is not the case for conventional analyzers, where the resolution in one coordinate is often reduced due to a finite width of the entrance slit. Even when we are only interested in the band dispersion $E(k_{||})$, always a complete 3D data set (E_B, k_x, k_y) must be recorded by taking a series of images at different E_B. Such measurement contains the full information about the band dispersion $E(k_{||})$ along any crystallographic direction. We note that the acquisition time for each E_B of this series can be set to be considerably shorter, compared to Fig. 21(a). The sharp band dispersion of the surface state, shown in Fig. 21(b), was extracted from a measurement with a time of 30 s per energy (i.e., 30 times faster than Fig. 21(a)) and in E_B steps of 10 meV, resulting in a total acquisition time of 30 min for the complete 3D (E_B,k_x,k_y) data set. This shows that the time required to measure even the complete band dispersion is comparable to the time for the high resolution Fermi surface map in Fig. 21(a). This is possible, as we select the cut along the horizontal k_x axis such, that intensities are binned over $k_y = 0 \pm 0.025$ Å^{-1}, similar to the finite $\Delta\theta_\perp$ of conventional ARPES analyzers. Under these practical conditions, both images (Fig. 21(a) and (b)] have a similar number of integrated counts. We note that still a complete 3D (E_B, k_x, k_y) dataset was recorded during the 30 min acquisition time. It is possible to extract different sections along arbitrary $E(k_x,k_y)$ crystallographic directions after the measurement to be compared with detailed theoretical band calculations. In combination with much brighter photon sources, like lasers and undulator synchrotron radiation, the measurement efficiency can be further increased.

It was shown recently for pulsed light excitation, that the sequential energy filtering might be replaced by the time resolved detection of electrons after passing a low-energy drift tube. This time-of-flight (ToF) spectroscopy was previously demonstrated for PEEM [80]. Electrons with different E_B will arrive at different times at the detector, and the arrival time can be directly converted to the energy. Unlike other energy filters, where only electrons of a selected energy are transmitted, the ToF analyzer therefore allows to record a certain energy window simultaneously. This energy window is typically a few 100 meV up to a few eV wide. With modern detectors system like a delay line detector, up to 200 energy slices can be resolved in this energy window. It is important to note that the ToF analyzer is usually realized as a straight drift tube, and therefore the full image information, like the PEEM image or the (k_x, k_y) momentum image, also will be resolved. In ToF momentum microscopy [81,104] the simultaneous detection of all electrons results in a 3D map (E_B,k_x,k_y) of the photoelectrons in a single exposure of a few minutes. In the future, this simultaneous detection scheme of the full three-dimensional band dispersion will allow the investigation of samples that have very short lifetimes, e.g., at low temperatures, or where only low intensities are available, like in HAXPES. We note that the ToF principle works best when the repetition rate of the excitation source is low (e.g., <10 MHz), as for higher rates the time-dispersed electron spectrum in the drift-tube would overlap. When using such intrinsically pulsed excitation sources, for instance based on lasers, the combination of ToF momentum microscopy with novel imaging spin filters (see Section 8) might result in a huge boost of the measurement efficiency of spin resolved electronic structures.

7.3. SX- and HAX-ARPES by high-energy momentum microscopy

As already discussed in Sections 7.1 and 2, momentum microscopy by use of an imaging energy filter (tandem HDAs) combined with a properly designed momentum microscope input lens optics and decelerating lenses after the imaging energy filter can collect undistorted (k_x,k_y) momentum images at different E_B with very high efficiency. Since the photoionization cross sections of various orbits decrease dramatically with $h\nu$ beyond few hundreds eV as explained in Sections 3 and 4, high detection efficiency of the momentum microscopy is very attractive for high accuracy ARPES in the soft X-ray and hard X-ray regions.

Due to the high $h\nu$ in a HAXPES experiment, photoelectrons from the valence band are emitted with kinetic energies of several keV. Nevertheless, the spectroscopy in the valence band near the Fermi energy requires a rather good energy resolution of better than ~200 meV. It is known as the recoil effects and Debye-Waller factor broaden the (E_B, **k**) as discussed in Section 4. A major issue in typical HAXPES setups is the retardation of the high kinetic energy of the photoelectrons to the low pass energy of the spectrometer. Using a momentum microscope setup as shown in Figs. 20 and 16, strong acceleration–retardation of electrons is an inherent property of the PEEM objective lens. This is because the sample is immersed in a strong electric field that accelerates the electrons to energies of several 10 keV along the lens axis and electrons are then decelerated in every experiment to the low pass energy of the energy filter in the order of few 10 eV. As the sample is completely immersed in the accelerating field of the objective lens, we only need to consider the relative potentials of the sample and the microscope. That means, instead of floating the complete analyzer on a potential close to the kinetic energy of the electrons – as is done in most HAXPES setups – it is sufficient here to apply a positive bias to the sample [82]. This in general works as long as $E_{kin} \ll U_A$. With a practical value of $U_A \sim 30$ kV for a high energy set up, photon energies of several keV can be used.

The similarity of a momentum microscope optics to a PEEM lens allows to perform HAXPES in a spectroscopic PEEM experiment, for instance to measure spatial maps of the elemental composition of a sample, making use of the enhanced bulk sensitivity of HAXPES. Fig. 22 shows a HAXPES measurement, using 6.5 keV photons from

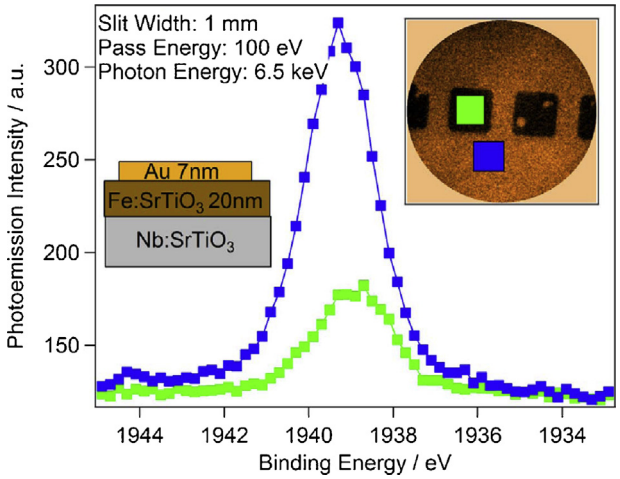

Fig. 22. Hard X-ray photoemission ($h\nu = 6.5$ keV) spectro-microscopy of Au contacts (dark square regions) on $SrTiO_3$. The green and blue spectra show the Sr $2P_{3/2}$ core level peak on the 7 nm Au layer and on the substrate. Inset top right: Energy filtered PEEM image (field of view 40 μm) recorded at the Sr 2p core level, and region of interest selected for the spectra (green and blue squares). Inset left: Sample layer composition [82].

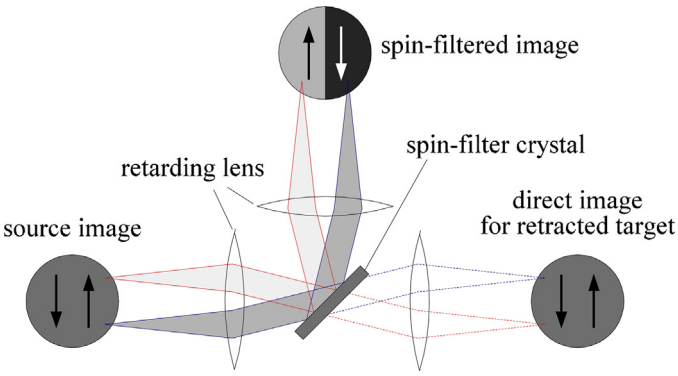

Fig. 23. Scattering geometry for the specular reflection of electrons at the spin-polarizing electron mirror (spin filter crystal). Scattering takes place under parallel beam conditions, preserving the spatial information of the source image. The spin-integrated image is obtained by retracting the target crystal [86].

the PETRA III storage ring, of $10 \times 10\,\mu m^2$ Au square contacts on a $SrTiO_3$ substrate [82]. The energy filtered PEEM image for the Sr $2p_{3/2}$ photoemission peak directly provides an element selective map of the selected peak (please refer to the figure caption). The Au covered area appears dark, due to the attenuation of photoelectrons passing through the 7 nm Au layer. Spectra taken in the different areas reveal a clear contribution of the substrate peak even in the Au covered area, indicating the bulk sensitivity of HAXPES. The local spectroscopy reveals that the photoemission peak from the uncovered surface is found at 0.4 eV higher E_B compared to the Au covered area. This result indicates that interfacial states at the metal electrode differ from the bulk electronic states and may contribute to a better understanding of the role of the interface region in such resistive switching materials [83].

As we pointed out before, momentum images recorded by the momentum microscope are always characterized by a constant linear scale in the k_x and k_y directions, independent of the selected energy. This is also the case for energies in the hard X-ray range. This is an important advantage of the momentum microscope for momentum resolved measurements at these energies. By contrast, conventional spectrometers resolve a fixed emission angle, and at high E_{kin}, photoelectrons form the first Brillouin zone are emitted into a narrow cone. This is seen, for instance, in Fig. 9(c) where the measured angle interval spans many BZs, at the cost of a low resolution in $k_{||}$. With a momentum microscope, however, the $k_{||}$ resolution is nearly constant at all E_{kin}. In detail, it was shown that the resolution limiting aberrations introduced by the PEEM objective lens even become lower at higher kinetic energies of the photoelectrons [84]. We note, however, that the use of a momentum microscope for the HAX-ARPES experiment does not impose a fundamental limit to the accessible k-space to the first or second BZ. Instead, designs of the objective lens optimized for high electron energies can provide (k_x,k_y) images up to $\pm 25\,Å^{-1}$ as shown in Ref. [85]. At $h\nu = 5$ keV, this corresponds to a collection angle of $\pm 45^\circ$.

8. Imaging spin filters and multi-channel spin detection

8.1. The working principle of imaging spin filters

Recently, electron spin detection has also been boosted by the introduction of the concept of multi-channel spin analysis, measuring more than one data point at the same time. Similar to conventional single-channel spin detectors, the principle of multi-channel spin detection is based on a spin selective scattering process. However, the traditional one-channel (or single-channel) spin detector has been replaced by a virtual array of spin detectors (up to several thousands). Practically, this was accomplished by developing the "spin-polarizing electron mirror", which allows the measurement of spin-resolved images of a two-dimensional electron distribution. This two-dimensional distribution can be either the high-resolution spatial image of a photoelectron emission microscope (PEEM) [86], or the intensity distribution in the exit plane of an energy-dispersive analyzer [87], or the *k*-image of a momentum microscope [8,88].

Fig. 23 shows the scattering geometry of such an imaging spin filter. Incoming electrons from different points in the source image are transformed by electrostatic electron lenses into a multitude of small parallel beams. These beams are diffracted from a spin selective single crystal surface in the specular geometry. Here, the two-dimensional image information is encoded in small variations in the angel of incidence onto the mirror. Among the many LEED reflections, the (0,0) beam is the only one which conserves the momentum parallel to the surface for elastic diffraction. After diffraction the individual beams are recombined by a second electrostatic lens, and an image of the electron source distribution is generated on a 2D-multichannel detector.

Spin contrast is obtained due to the spin dependent reflectivity of low-energy electrons at the non-magnetic surface of the scattering target being governed by spin-orbit coupling, such that electrons with opposite spin see different scattering potentials, leading to different scattering amplitudes [89]. In this way the spin polarization distribution in the primary beam is translated into an intensity distribution at the 2D detector, and the spin-polarizing power of the electron mirror is equal to the intensity asymmetry upon reversal of the primary beam polarization. Different target crystals exist for use in the imaging spin-filter.

The first demonstration of the imaging spin-filter employed a W(0 0 1) single crystal surface [86,87]. This target is characterized by an easy and reproducible preparation procedure and a quite high efficiency per channel. However, this system has the practical inconvenience that it requires frequent cleaning of the surface [52,53]. This stability probrem was slightly improved using an Ir(0 0 1) surface, which however exhibits a 5×1 reconstruction [90]. It was finally shown recently, that this reconstruction is absent on the surface of a pseudomorphic monolayer of Au grown on Ir(0 0 1) [88,91]. The 1 ML Au/Ir(0 0 1) system combines a high spin-sensitivity and high reflectivity, even superior to the W(0 0 1) surface, with a long-term stability of more than

several weeks. At present, this makes the 1 ML Au/Ir(0 0 1) system the primary choice for an imaging spin-filter for high resolution applications.

We note that the conservation of parallel momentum upon diffraction in the (0,0) LEED beam of the crystal surface is equivalent to the reflection of photons at an optical mirror. Each electron that was reflected from the surface originates from the spot where the primary electron did impact on the surface, and the angle after the scattering is equivalent to the angle of incidence, but mirrored. This analogy with an optical mirror shows that, in principle, an ideal electron mirror can be placed anywhere in the electron optical path, still preserving the image information. Most importantly, this means that the image resolution does not rely on the precise position of the intermediate reciprocal image in Fig. 23 on the crystal surface, which is inclined by 45° with respect to the image plane.

Real crystals are, however, characterized by imperfections that lead to an angular broadening of the diffracted beam, and the fundamental limitation of the image resolution is imposed by the crystal quality of the target. A major source of this angular broadening is the mosaicity of the real crystal. For instance, a typical mosaic-spread of a tungsten crystal is in the order of 0.05°–0.1°. This means that a parallel beam will be diffracted into a cone of a width 0.1°. It was found experimentally, that this angular broadening is in good agreement with observed resolution in the order of 70 × 70 resolvable points in a spin-filtered Image [86]. We also note that a finite angular broadening also means that the obtainable image resolution is not anymore totally independent from the target position with respect to the intermediate image planes, in contrast to the case of an ideal electron mirror. In the limiting case of a completely diffuse scattering target, image information can only be preserved by placing the crystal exactly in a focused image, while the angular coordinate is lost. This, however, is not exactly possible in the 45° inclined geometry, and poses the additional complication that the 2D image information is superimposed by defects of the crystal surface. Therefore, applications that take the advantage of a high resolution spin filtered image, like the spin-resolving momentum microscope, prefer single-crystalline spin-filter targets like the W(0 0 1) and Au/Ir(0 0 1) systems with a specular reflection of the (0,0) LEED beam.

Fig. 20 also shows the effective application of an imaging spin filter – here using the Au/Ir(0 0 1) target – in a spin-resolving momentum microscope system. The momentum microscope allows the efficient simultaneous measurement of both in-plane momentum coordinates (k_x, k_y) of the photoelectrons, in a high-resolution image. The details of this novel approach to band structure imaging is discussed in detail already (Section 7). The spin-filter, as shown schematically in Fig. 23, is installed at the exit of the imaging energy filter. Note the schematic decelerating and accelerating electrostatic lenses before – and after – the Ir spin-filter crystal, used to guide the electrons and adapt their kinetic energy from the pass-energy of the energy filter to the – typically lower – scattering energy at the crystal. (In a real instrument, additional electron lenses might be used, for instance, to adapt for image sizes on typical MCP detectors.)

In addition to this type of advanced use in a momentum microscope, imaging spin-filters (W(0 0 1) or Ir(0 0 1) electron mirror) were successfully used behind HDA of a conventional ARPES system [87,90]. There, the high measurement efficiency provided by the multi-channel approach allowed one to study systems which are known for a short lifetime, due to a high surface reactivity. A particular example is the surface of Heuser alloys, where the predicted half-metallicity is usually not found in spin-resolved UPS experiments, a discrepancy which might be circumvented by reduced measurement times using imaging spin filters [92]. Related to the large exit window of the analyzer and the energy

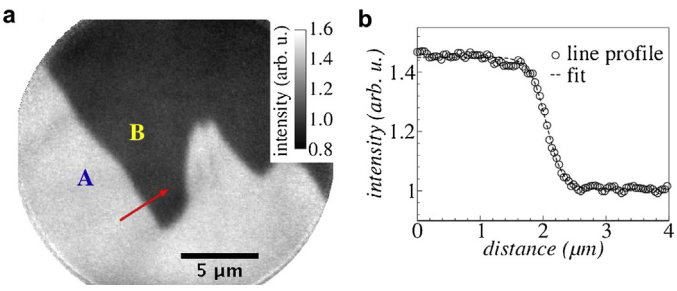

Fig. 24. (a) Spin filtered PEEM image of magnetic domains in an 8 ML cobalt film on Cu(1 0 0). (b) Intensity profile over the boundary between domains A and B [86].

dispersion in one direction, however, the image projection commonly faces additional issues like the chromatic aberration, in this case [87,90]. In contrast to the combination with a momentum microscope, a somewhat lower number of channels might be obtained. For instance, Ref. [87] showed that a total of 64 angular points × 17 energy point, i.e., 1044 data points were acquired simultaneously. This is a somewhat lower efficiency gain as for the first demonstration of the W(0 0 1) electron mirror in combination with monochromatic images from the electron microscope [86]. Nevertheless this represents a giant boost in spin detection efficiency for ARPES experiments, compared to conventional single-channel spin polarimetry. Detailed considerations of the detection efficiency will be given below.

Besides the imaging spin filter, other approaches to combine spin resolution with multi-channel detection exist. It was demonstrated that ToF energy analyzer can be combined with a conventional spin detector, for instance of the Mott type [93], or using exchange scattering at the Fe(0 0 1)-$p(1 \times 1)$—O target [94]. Compared to the imaging spin-filter, only one coordinate axis, the energy, is detected simultaneously, and the efficiency gain in this 1D spin detection is typically two orders of magnitude lower that for 2D image spin detection. We like to note that this ToF detection principle can be combined with almost any kind of spin-polarimeter. In particular, a PEEM with a ToF energy analyzer [80] or a momentum microscope with ToF energy separation [81,104] might be combined with an imaging spin filter using the specular reflection from a W(0 0 1) or Au/Ir(0 0 1) target. This will enable the completely simultaneous 3D (k_x, k_y, E_B) acquisition of spin resolved data sets with more than 10^5 (k_x, k_y, E_B) data points.

8.2. Spin-resolved photoelectron emission microscopy

An application that makes direct use of the imaging properties and high efficiency of the imaging spin filter is spin resolved photoelectron emission microscopy. Opposite to surface microscopy techniques that probe the magnetic information in the excitation step, like PEEM with X-ray magnetic circular dichroism (XMCD) [95–97], or spin-polarized low-energy electron microscopy (SP-LEEM) [98], the spin filtered PEEM provides a direct analysis of the spin of the emitted photoelectrons. It therefore provides complementary information to element selective XMCD.

Spin filtered PEEM images can be measured in a momentum microscopy setup like that shown in Fig. 20, when this instrument is switched to image the microscopic real-space surface of the sample, instead of the (k_x,k_y) momentum distribution. In this way, spin-resolved micro-spectroscopy of the valence band region becomes possible, with a typical PEEM resolution in the order of <100 nm. Fig. 24(a) shows an example of a spin filtered PEEM measurement of an 8 ML thick cobalt film on Cu(1 0 0) [86]. In that case, the surface was excited with photon pulses from a femtosecond laser source, while the non-linear 2-photon photoemission of the resonant excitation through the spin polarized quantum well [99]

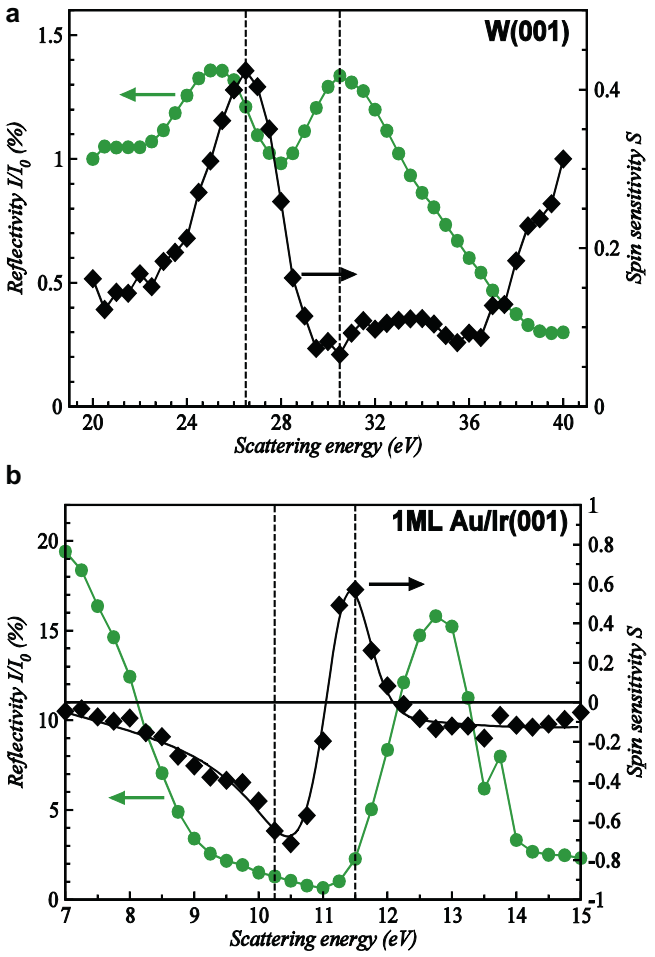

Fig. 25. Spin averaged reflectivity (I/I_0, left), and spin sensitivity (S, right) for different spin filter crystals, as a function of the electron scattering energy. (a) Curves for the W(0 0 1) spin filter crystal with working points at a scattering energy of 26.5 eV and 30.5 eV [100]. (b) The same for the pseudomorphic monolayer of Au on Ir(0 0 1) with working points at 10.25 eV and 11.50 eV [88]. These working points were selected by considering (1) small mutual energy difference, (2) high spin sensitivity with plus and minus sign and (3) much higher reflectivity compared with those at higher scattering energies (Fig. 26).

state was detected. Due to the high spin-asymmetry of 42% of the W(0 0 1) mirror, the magnetic domains are directly visible in the intensity image as a black-white contrast. The intensity profile in Fig. 24(b) reveals the intensity difference between the magnetic domains A and B. The measured width of the transition of 500 nm is limited by the domain wall width in the cobalt film, which is characterized by a low magnetic anisotropy.

8.3. Types of scattering targets for the imaging spin-filter and their properties

The first demonstration of imaging spin-filters used a clean W(0 0 1) single crystal surface as the electron mirror. Fig. 25(a) shows the variation of the spin-sensitivity (S) and the spin-averaged reflectivity $R = I/I_0$ as function of the scattering energy. From these curves, two working points at 26.5 eV and 30.5 eV with a high reflectivity were identified. It was shown that quantitative spin-resolved data can be obtained by measurements at both working points, switching S between 42% and 5% [100]. We note that at $E_S = 26.5$ eV the reflectivity was found to be 1.2%, such that a single-channel figure of merit of $f_0 = S^2R = 2.1 \times 10^{-3}$ was found. This value is already one order of magnitude larger than widely used Mott- or conventional SP-LEED analyzers. With a total number of $N = 3800$ resolvable image points, an effective 2D figure-of-merit $F_{2D} = 8.0$ was obtained. The use of clean W(0 0 1) is, however, connected with the practical inconvenience that it requires frequent cleaning of the surface due to hydrogen adsorption which degrades the spin analyzing power [52,53].

By using an Ir(0 0 1) single crystal, the lifetime of the spin filter between preparation cycles could be considerably improved [90]. Recently, high spin-polarization together with a high reflectivity was reported for the elastic electron reflection at an Ir(0 0 1) surface, which was passivated by a pseudomorphic monolayer of Au [91]. The preparation of this Au monolayer follows a straightforward procedure by deposition of Au onto the clean Ir(0 0 1) – 5 × 1. In an annealing step, the excessive amount of Au is desorbed such that only the stable monolayer is left on the surface, which has a higher desorption temperature. The pseudomorphic monolayer is characterized by an unreconstructed (1 × 1) diffraction pattern. Under UHV conditions, a long term stability of the Au/Ir(0 0 1) surface over more than 6 months was reported [88].

Fig. 25(b) shows the measured reflectivity and asymmetry for this Au/Ir(0 0 1) spin filter. This reveals a very favorable property of this system: A high spin sensitivity is connected with the reversal of the sign from −60% to +60% within the energy interval from 10.25 eV to 11.5 eV. It was found that the sign reversal at these energies is related to an interference of scattered LEED beams at the surface barrier [88]. The reflectivity at these two asymmetry maxima is 1.3% and 2.2%, respectively. This is considerably better than for W(0 0 1), increasing the figure-of-merit of $f_0 \sim 7 \times 10^{-3}$ per point, which is among the highest values reported so far for single-channel detectors. With a momentum microscope setup as in Fig. 20, spin resolved images with 5000 resolvable points were demonstrated, which results in an effective $F_{2D} = 37$ [8,88]. We also note the additional advantage of the reversal of the sign of the asymmetry within a small energy interval. Subsequent measurements at two scattering energies facilitates the quantitative analysis of spin-resolved momentum images. Due to the sharp polarization peaks, this working point can be efficiently used for the acquisition of monochromatic images.

So far, the imaging spin-filters used a scattering geometry with an angle of incidence around 45°. However, there is no fundamental restriction to this particular angle. As the maxima and minima in intensities and asymmetries are governed by multiple scattering of the low-energy electrons, there exists a rich landscape of such pronounced maxima and minima, which is not straightforward to predict. Two-dimensional energy vs. angle landscapes can be obtained using a spin-polarized electron diffraction setup consisting of a spin-polarized electron source [101], a goniometer for the crystal and a movable detector. Such measurements were performed for clean W(0 0 1) [102], Fe(0 0 1)-p(1 × 1)—O [57], and Au/Ir(0 0 1) [91]. Fig. 26(a) and (b) shows such measurements for the 1 ML Au/Ir(0 0 1) system. In the spin asymmetry we find numerous regions of high positive and negative asymmetry. This map shows that also regions exist where the asymmetry does not change for lager energy intervals. Such regions might be interesting in combination with conventional ARPES analyzers or ToF spectrometers where a larger energy window needs to be transmitted, than for monochromatic images of a momentum microscope.

Fig. 26(c) and (d) shows the same values calculated in a spin-polarized relativistic layer Korringa–Kohn–Rostoker (KKR) approach [103]. The theory shows remarkable agreement with the experimental results, reproducing even tiny features and the points of reversal of the asymmetry. This is particularly useful for a better understanding of the underlying electron scattering. In the future, this will lead to further improvements of the detection efficiency of the imaging spin-filters, for instance by the search for new target materials and optimizing scattering conditions.

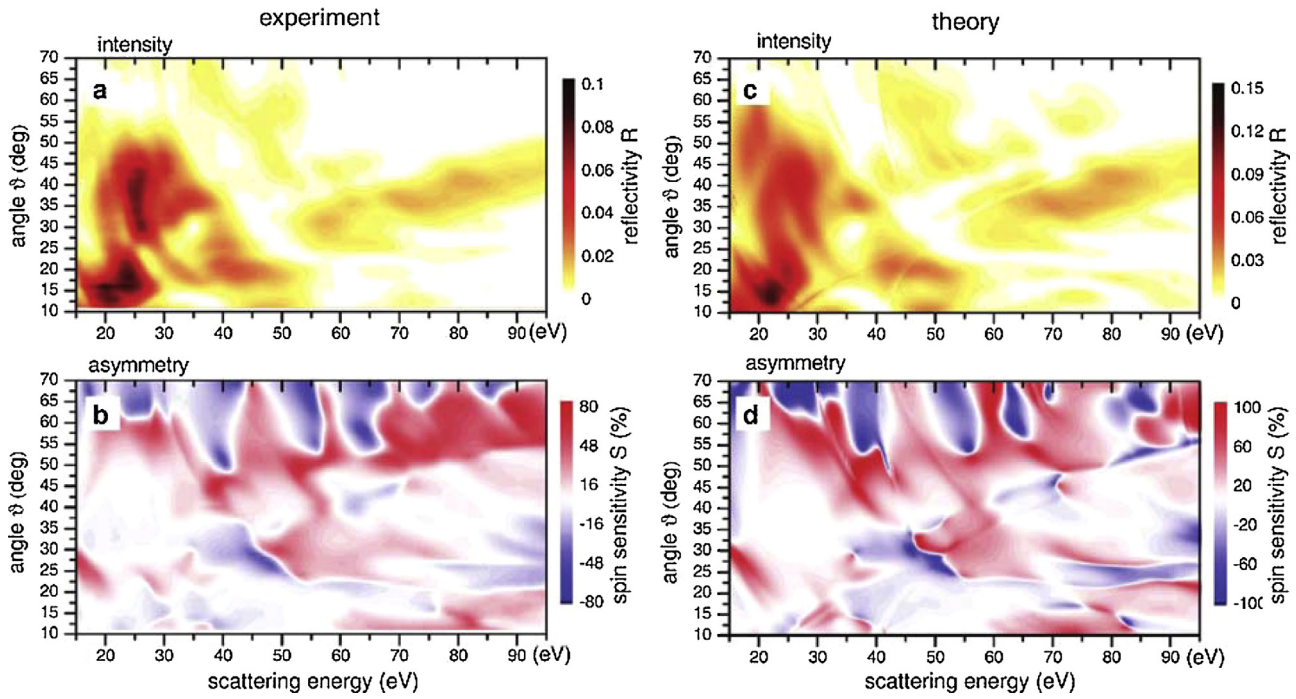

Fig. 26. Specular reflection of spin-polarized electrons from a pseudomorphic monolayer of Au on Ir(0 0 1) as function of scattering energy and polar angle of incidence on the crystal surface along the azimuth. (a) and (c) reflectivity I/I_0. (b) and (d) spin sensitivity S. The left panels (a) and (b) show the experimental results and the right panels (c) and (d) calculated maps by means of a relativistic layer Korringa–Kohn–Rostoker (KKR) approach [91].

8.4. *The measurement principle using imaging spin-filters*

After the spin filter, typically two detector arms are used. In the straight-through direction, the detector records spin integrated images. For this purpose, the spin-filter crystal is mounted on a retractable manipulator, such that it can be removed from the beam path (Fig. 20). In that case, with a proper design of the electron optics there is no deterioration of the image resolution compared to a system which does not include the spin-filter part. For spin filtered measurements the detector arm at the angle of 90° is used. As noted above, the spin selective reflection at the crystal surface leads to a variation in the intensity at the detector depending on if the spin is pointing *up* or *down* along the quantization axis **P**. As for spin-orbit scattering in general, this quantization axis is aligned perpendicular to the scattering plane spanned by the incoming- and reflected-beam directions [4].

This situation is somewhat different from the widely used Mott- or conventional SP-LEED detector that have two electron counters, one having a higher (lower) sensitivity for the spin-up (spin-down) direction (Fig. 12). In the case of imaging spin-filters, we need in general two measurements to extract the information about the photoelectron spin-polarization. This is similar to single-channel detectors based on the exchange scattering principle, where the magnetization direction of the target can be reversed (Fig. 13), whereas this is obviously not possible for spin-orbit scattering.

An obvious solution for that issue would be to take two images, one at the spin-integrated and one at the spin-filtered detector arm. A second possibility would be to install a third detector arm in the opposite scattering direction, such that the spin-orbit asymmetry gets reversed. While both of this solutions would allow the extraction of quantitative spin information, they require mechanical realignment between the measurements and use different detectors with possibly different sensitivities. Then as in other detectors that use different electron path and detectors for spin-up and spin-down electrons, systematic instrumental asymmetries are induced [6].

A more practical solution to quantitatively determine the total intensities and the spin polarization at every point of the spin-resolved image was introduced in Ref. [100]. This procedure makes use of the variation of the spin-sensitivity as a function of the scattering energy. In Fig. 25, we already showed these curves for W(0 0 1) and Au/Ir(0 0 1) spin-filter targets. For the latter one, we see that the spin-sensitivity even can be reversed by changing the scattering energy by only 10%. Images that contain mostly spin-up or mostly spin-down partial intensities therefore can be recorded one after the other by changing the Au/Ir(0 0 1) potential. A practical advantage is that all electrons travel along the same path inside the electron optics, and the same detector is used.

Fig. 27(b) and (c) shows the camera images that were recorded in the spin filtered detector arm after the electrons were reflected from a 1 ML Au/Ir(0 0 1) surface [88]. This measurement, acquired with the momentum microscope setup in Fig. 20, shows the Fermi surface map of the surface state on Au(1 1 1). The surface state is separated into two rings due to the Rashba type spin-orbit splitting. It is well-known that the spin-polarization vectors run along two circles in opposite sense, lying in the surface plane [78,79]. The images (b) and (c) were recorded at different scattering energies that correspond to negative or positive spin-sensitivity. We note that the sample was illuminated by a laboratory gas discharge lamp (He-I line) and each image was only integrated for 15 min. Due to the large spin-sensitivity of the Au/Ir(0 0 1) surface in the order of ±65%, the contrast is reversed between the images (b) and (c) and they are closely related to the spin-resolved partial intensities. This is, however, only an approximation, and a general procedure to derive quantitative results was introduced in Ref. [100]. For this procedure, two measurements are taken, one at the low (l) and one at the high (h) scattering energy. In the above

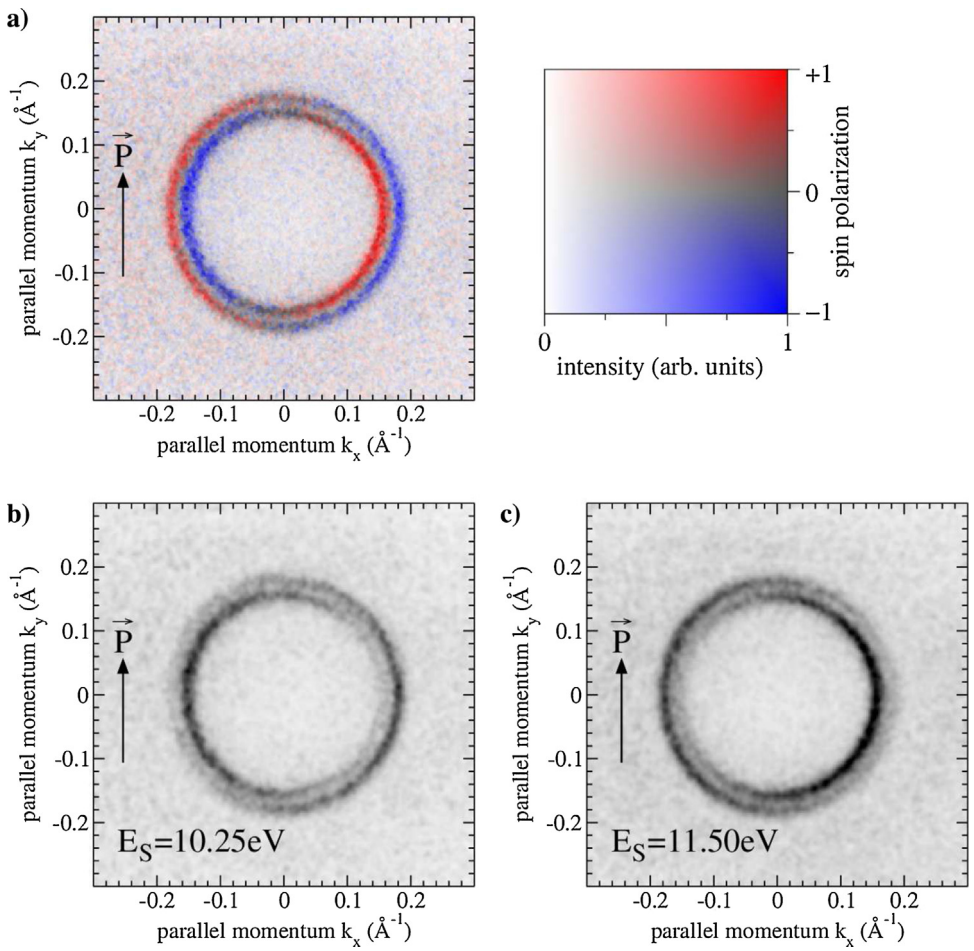

Fig. 27. (a) Spin resolved Fermi surface map of the Rashba split surface state of Au(1 1 1) with respect to the quantization axis indicated by **P**. Note the two-dimensional color code for intensity and spin polarization. (b) Intensity distribution after the spin-polarizing mirror at 10.25 eV scattering energy (c) Intensity distribution at 11.50 eV scattering energy. Note the complementary black-and-white contrast in (b) and (c) [88].

example, this corresponds to the image at 10.25 eV and 11.5 eV, respectively. When the photo current at each image coordinate is $I_0(x,y)$ and the spin polarization is $P(x, y)$, the intensity measured at both scattering energies is

$$I_l(x, y) = I_0(x, y)\,[1 + S_l P(x, y)]\,R_l(x, y) \tag{8.1}$$

and

$$I_h(x, y) = I_0(x, y)\,[1 + S_h P(x, y)]\,R_h(x, y) \tag{8.2}$$

It was demonstrated that the spin sensitivity $S_{l,h}$ at both working points of the W(0 0 1) and Au/Ir(0 0 1) spin filter targets does not change significantly over the image, while the spin-averaged reflectivity $R_{l,h}(x,y)$ is a position dependent quantity. The $R_{l,h}(x,y)$ can be determined in situ, for instance, by measuring distributions of unpolarized electrons. Solving Eqs. (8.1) and (8.2) for the unknown quantities I_0 and P, we arrive at

$$P(x, y) = \frac{J_l(x, y) - J_h(x, y)}{S_l J_h(x, y) - S_h J_l(x, y)} \tag{8.3}$$

and

$$I_0(x, y) = \frac{S_l J_h(x, y) - S_h J_l(x, y)}{S_l - S_h}, \tag{8.4}$$

where $J_{l,h} = I_{l,h}/R_{l,h}$ is the measured intensity image $I_{l,h}$ normalized to the reflectivity reference image $R_{l,h}$ for the low (l) or high (h) scattering energy working point, respectively [8]. We note that this is a generalized expression compared to the asymmetry, A, introduced earlier (see Section 6). For instance, if we take the indices l and h as the left and right detectors of a conventional Mott or SP-LEED type detector, the reflectivity would become to $R_l = R_h = I/I_0$, and the spin-sensitivity would become $S_l = -S_h = S$ (note the opposite sign). Inserting this in Eq. (8.3) results in the well known expression $P = A/S$, with the measured asymmetry A. This, however, neglects instrumental asymmetries that are present in real systems. In conventional spin detectors such as Mott or SP-LEED type, for example, equality of intensities and spin-sensitivities cannot be assumed, in general. In practice, Mott-type detectors are particularly sensitive for instrumental asymmetries due to their low value of the Sherman function. Then corrections have to be made experimentally by a proper calibration procedure [93]. In the case of the imaging spin-filter, on the other hand, instrumental influences of R and S are already included in Eqs. (8.3) and (8.4), such that no further corrections are required.

Fig. 27(a) shows the intensity and spin-polarization of the photoelectrons leaving the crystal with the component of the polarization vector along the direction of the **P**-arrow. This is the result after the analysis, where we employ a 2D color code for the intensity and the degree of polarization. Note that we see two circles of varying color and intensity. The colors are opposite in the left and the right halves and fade out in color along the vertical line in their middle. This indicates that the electrons with $k_x = 0$ have a vanishing spin-polarization projection along the P direction whereas the electrons with $k_y = 0$ have a maximum projection, changing sign on going from negative k_x to positive k_x.

8.5. The efficiency of multi-channel and imaging spin-filters

The most important reason to use imaging- or other multi-channel spin-filters is to realize a high gain in efficiency that speeds up the collection of spin-resolved data. It is of course interesting to quantify the gain in efficiency, comparing different kinds of detectors. For single-channel detectors, the efficiency is expressed by the figure-of- merit, $f_0 = S^2I/I_0$. This number can be interpreted as the rate at which experimental data points are collected, compared to the collection of one spin-averaged data point with the same statistical error. Namely, the acquisition time of a single data point needs to be increased in the spin-resolved experiment. For instance, when a spin-averaged data point is acquired in the time t_0, acquisition of the spin-resolved data point takes a time $t = t_0/f_0$. The figure-of-merit is usually a small number $f_0 = 10^{-4}$–10^{-2} for single-channel detectors.

When we replace the single-channel detector by a large number (N) of (virtual) detectors, each of this N detectors will acquire one data point during the time t. While each of the channels is characterized by the respective single channel efficiency f_0, the rate at which experimental data points are collected is increased by the factor of N. Therefore, the efficiency $\boldsymbol{F}_{2D}$ of the imaging detector was defined as the rate at which data points are collected: $\boldsymbol{F}_{2D} = (t_0/t)\,N$. With $f_0 = t_0/t$ from above, we can write this 2D detection efficiency as:

$$\boldsymbol{F}_{2D} = \langle f_0 \rangle\, N, \tag{8.5}$$

where $\langle f_0 \rangle$ denotes the average f_0 over the complete image. We note that a single- channel detector with $N = 1$ will have a detection efficiency of $\boldsymbol{F}_{2D} = f_0$. Therefore, we can directly compare the efficiency of different detectors to record a 2D data set. For instance, the measurement of a 2D intensity distribution–which can be a $E_B(k_x,k_y)$ map, or a (E_B,θ) distribution, or a PEEM image—using a detector with $F_{2D} = 8$ [86] is 8×10^4 times faster than the measurement of the same image using a Mott detector with $f_0 = 10^{-4}$ in scanning mode. We note that this comparison assumes that the single-channel detector is set to the same resolution as for the measurement with the 2D detector. In a practical case, however, the low efficiency of a single-channel detector usually requires a compromise in resolution setting in order to perform the realistic measurement. Therefore the use of an imaging spin-filter will result in a much higher resolution, under practical conditions.

The channel number N should be understood as the number of statistically independent data points that are collected within one image. For instance, in Ref. [87], 64 points in the θ coordinate, and 17 points in the energy scale were resolved simultaneously, resulting in $N = 1044$. In Ref. [86], 70 points over the diagonal of a PEEM image were resolved, which results in $N = 3800$ in the circular field of view. As a general expression, the number of channels in an n—dimensional dataset can be written as:

$$N = \prod_{i=1}^{n} \frac{\Delta X_i}{\langle dX_i \rangle} \cdot \Omega, \tag{8.6}$$

where ΔX_i is the simultaneously acquired interval along the coordinate axis X_i (this can be one of E, θ, x, y, k_x, k_y, etc.), and $\langle dX_i \rangle$ is the average resolution along this axis. The total N is derived by multiplying the point numbers of the individual multichannel coordinate axes N_i for $i = 1$ to $i = n$. The additional factor Ω accounts for the shape of the image, i. e., 1 for a rectangular field of view, $\pi/4$ for a circular field of view, etc. This consideration shows that a detection efficiency, $\boldsymbol{F}_{n\mathrm{D}}$, can as well be defined for other multi-channel detectors. Examples are one-dimensional detectors like the ToF type [93,94], or 3D detectors like a combination of ToF with an imaging spin-filter [104].

9. Conclusion and prospect

By today, conventional ARPES spectrometers are based on a single HDA, where a 2D detector simultaneously records the binding energy E_B and emission angle θ along a certain direction. After converting θ to the surface parallel momentum $k_{x,y}$, the band dispersion is obtained along one crystal axis. In addition to the numerical treatment of the data to obtain $k_{x,y}$ from θ, a major limitation of this conventional approach is that large regions of the surface Brillouin zone in the (k_x,k_y) plane cannot be easily covered. Such measurements usually require time-consuming mechanical rotation of the sample or analyzer, and accuracy and reproducibility as well as maintaining a fixed position of the focused photon beam on the sample pose major experimental challenges.

The concept of momentum microscopy, as discussed in Sections 7.1 and 7.2, uses a different approach than the conventional ARPES: Based on the electron optical properties of a PEEM lens, electrons emitted from the sample surface in all directions are simultaneously collected, and imaged on the 2D detector. These "momentum images" are always scaled linearly in the k_x and k_y coordinates, and represent a direct view of the reciprocal space, for instance, as a section through the Fermi surface of the sample. As no mechanical movements of the sample are required, more than the complete surface Brillouin zone can be simultaneously covered in a single acquisition, keeping the beam spot exactly at the same sample position, and enabling experiments with high spatial resolution. The selection of E_B is accomplished by an imaging energy filter, which is commonly an S-type arrangement of two HDAs. By scanning the exit electron energy, $E_B(k_x,k_y)$ maps can be obtained with high k resolution of $<5 \times 10^{-3}$ Å^{-1} and high energy resolution of 12 meV over a wide energy- and momentum-space owing to the low image aberration. As a great advantage of this type of instrument, the momentum resolution does not become worsened even when the $h\nu$ is increased to soft and hard X-ray regions. Also many other types of imaging energy filters can be effectively used for momentum microscopy. A particular example is the ToF analyzer which can be used in connection with pulsed photon sources (e.g. laser, synchrotron radiation). In the case of ToF, resolution better than 10 meV can be expected. In practical terms, the cost (size and weight) of a ToF analyzer is usually much cheaper (smaller and lighter) than other imaging energy filters, and transportation between synchrotron radiation facility and laboratory becomes easier.

Although the detection of the photoelectron spin attracted many scientists for more than half a century [4], the low detection efficiency hindered its progress until recently till the high accuracy and high efficiency detection of the momentum dependent spin of photoelectrons became feasible. In order to compensate the low detection efficiency, the spin measurement of the photoelectrons was often performed without paying attention to the angular (momentum) resolution in the initial stage. The figure of merit f_0 for the single channel spin detection was up to 10^{-4} for few decades as shown in Fig. 28, where the evolution of the spin detection efficiency of various detector technologies over the past 5 decades is illustrated. The effective detection efficiency of the conventional single channel or 0D (zero-dimensional) detectors, like Mott, SP-LEED, or exchange scattering detectors, is equal to their Figure of merit, f_0. For multichannel detectors like the 1D ToF- or 2D imaging-spin detectors, the effective efficiency is the multichannel efficiency, F_{1D} or F_{2D}. We note that the efficiency of spin detection has increased by more than 5 orders of magnitude since the first introduction of Mott detectors to photoemission spectroscopy. Mott detectors, which have the lowest efficiency among these detectors are still the most commonly used type of spin detector in electron spectroscopy. The reason is their stable operation for a long period without deterioration and ease of use. Up to now

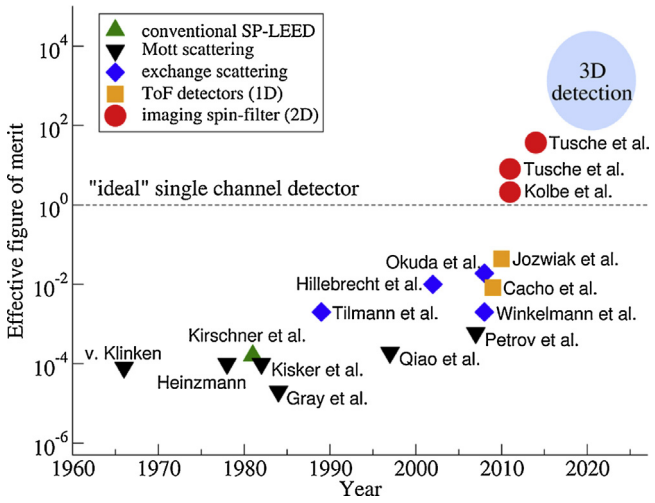

Fig. 28. Evolution of spin detection efficiency. Symbols show the effective figure of merit F_{nD}. F_{0D} ($n=0$: zero-dimensional) corresponds to f_0 of single-channel detectors based on Mott-, SP-LEED- and exchange-scattering. F_{1D} to detectors as time-of-flight (ToF) energy analyzer, and F_{2D} to imaging spin filters. Data from Refs. [5,7,8,55,86,87,93,94,106–113]. In cases where the multi-channel efficiency was not given, it was estimated from the data provided.

many Mott detectors of different designs were sold as commercial add-ons for electron spectrometers. Nevertheless, the need for improved spin detection efficiency for applications in high-resolution spectroscopy and SP-ARPES triggered the development of new detection schemes, like the SP-LEED detector or detectors based on exchange scattering from ferromagnetic materials. In fact, f_0 is nowadays much increased beyond 10^{-2} by using such a new target as Fe(0 0 1)-$p(1\times1)$—O, where the spin sensitivity is governed by exchange scattering. The useful lifetime of this spin detector is also prolonged for more than a month, and this detector is now very user-friendly.

In accordance with the increase of f_0 by 2 orders of magnitude in the recent decade, the angle resolved measurement of the spin of photoelectrons, called SP-ARPES, is becoming very popular nowadays to study the spin texture of materials like topological insulators [45,60]. Still the SP-ARPES by single-channel detection requires ~5 orders of magnitude longer measuring time than high-resolution ARPES without spin detection. How to improve spin detection efficiency was an important subject for decades of many scientists interested in SP-ARPES.

However, a tremendous boost of the efficiency of spin detection is triggered with the introduction of multi-channel detection. 1D detectors with ToF analyzers measure many energy channels simultaneously, resulting in an efficiency gain of 1–2 orders of magnitude, and 2D imaging detectors which measure a complete (E,θ) or (k_x, k_y) image with an efficiency gain of 3–4 orders of magnitude higher than the single-channel spin detection. We note that values $F_{nD}>1$ mean that these detectors are even more efficient than an "ideal" single-channel detector (like a hypothetical Stern–Gerlach spin separator) that would perfectly separate an electron beam in spin-up and spin-down without loss of intensity. More practically speaking, this also means that a spin resolved measurement with a 2D spin filter today is even faster than a spin-averaged measurement with a channeltron type detector in scanning mode, as it was used in early days of electron spectroscopy.

When an imaging spin filter such as Au/Ir(0 0 1) is combined with the momentum microscope, spin polarization at each (k_x,k_y) can be experimentally measured. Since the spin detection efficiency becomes N (number of total (k_x,k_y) channels) times larger than f_0, 2D spin detection efficiency F_{2D} can easily be more than 5 orders of magnitude higher than the case of single channel detection by a Mott detector and more than 3 orders of magnitude higher than the spin detection by a Fe(0 0 1)-$p(1\times1)$—O detector. Although the measurement of SP-ARPES by use of W(0 0 1) and/or Au/Ir(0 0 1) detectors has been performed from 6 eV up to low $h\nu$ soft X-ray region so far, there is no essential difficulty to extend its use to high $h\nu$ soft X-ray region and even to the hard X-ray region. Even though the photoionization cross sections of various orbits decrease dramatically with $h\nu$ beyond few hundreds eV as explained in Sections 3 and 4, the high F_{2D} of this type of instrument will overcome this difficulty and enables one to do a high accuracy SP-ARPES in the soft X-ray and hard X-ray regions.

Nowadays, the difference between the spin polarization in the initial state and the photoelectron spin is under a hot debate [105]. Therefore full utilization of the polarization of the incident light (left and right-handed circularly polarized light as well as two orthogonally polarized lights) of the synchrotron radiation and the lasers will be required for detailed studies. Although the angle of incidence of the excitation light has often been not normal to the sample surface and off the axis of the input lens attached to the electron energy analyzer, one can even excite the photoelectrons under normal incidence, i.e., parallel to the input lens axis, in the case of the instrument described in Fig. 20. With the high symmetry of such experimental setup, the effect of photo- excitation to the photoelectron spin will simply be clarified, and the genuine initial state spin will be experimentally revealed.

In the future, the full three-dimensional (3D) and simultaneous detection of (E_B, k_x, k_y) by the combination of momentum microscope, ToF energy analyzers and imaging spin filter will boost the efficiency by another 1–2 orders of magnitude, and spin resolved band structure measurements will be finally as efficient as today's best performing spin-averaging experiments. Instruments using a ToF energy analyzer are useful for pulsed light sources with short pulse width, facilitating dynamical studies of the electronic structure, including the electron spin. On the other hand, dispersive imaging energy filters, such as the double HDAs, are extremely useful for CW or quasi-CW light sources, where spin resolved studies with high energy and momentum resolution become possible. A new era of spin resolved photoelectron spectroscopy will be started soon and detailed full information on electron spin in the form of $P_{x,y,z}(E_B(k_x,k_y,k_z))$ will become available for many materials, promoting the nanospintronics in the near future.

Acknowledgements

Both authors deeply acknowledge J. Kirschner for scientific collaboration and stimulating discussions on spin detection of polarized electrons over decades. Without his continuous support backed up by his enthusiasm on spin detection, the progress of our spin spectroscopy may have been much delayed. S.S. also acknowledges T. Okuda and A. Kimura for scientific discussions. C. T. acknowledges G. Schönhense, J. Henk and A. Winkelmann for fruitful scientific discussions and A. Krasyuk, M. Ellguth, F. Thiele, and G. Kroder for experimental support.

References

[1] M. Cardona, L. Ley (Eds.), Photoemission in Solids I, Springer, Berlin, Heidelberg, 1978.
[2] S. Hüfner, Photoelectron Spectroscopy, Principles and Application, Springer, Berlin, Heidelberg, 2003.
[3] S. Suga, A. Sekiyama, Photoelectron Spectroscopy, Bulk and Surface Electronic Structures Springer Series in Optical Sciences, vol. 176, Springer, Berlin, Heidelberg, 2014.
[4] J. Kessler, Polarized Electrons Springer Series on Atoms and Plasmas, Springer-Verlag, Berlin, 1985.
[5] J.V. Klinken, Nucl. Phys. 75 (1966) 161.
[6] J. Kirschner, Polarized Electrons at Surfaces Springer Tracts in Modern Physics, vol. 106, Springer-Verlag, Berlin, 1985.

[7] T. Okuda, Y. Takeichi, Y. Maeda, A. Harasawa, I. Matsuda, T. Kinoshita, A. Kakizaki, Rev. Sci. Instrum. 79 (2008) 123117.
[8] C. Tusche, A. Krasyuk, J. Kirschner, Ultramicroscopy (2015), http://dx.doi.org/10.1016/j.ultramic.2015.03.020 (in press).
[9] Y. Saitoh, H. Kimura, Y. Suzuki, T. Nakatani, T. Matsushita, T. Muro, T. Miyahara, M. Fujisawa, K. Soda, S. Ueda, H. Harada, M. Kotsugi, A. Sekiyama, S. Suga, Rev. Sci. Instrum. 71 (2000) 3254.
[10] T. Tanaka, H. Kitamura, Nucl. Instrum. Meth. A 364 (1995) 368.
[11] S. Sasaki, Nucl. Instrum. Meth. A 347 (1994) 83.
[12] A. Sekiyama, T. Iwasaki, K. Matsuda, Y. Saitoh, Y. Onuki, S. Suga, Nature 403 (2000) 396.
[13] N.E. Bickers, Rev. Mod. Phys. 59 (1987) 845.
[14] S. Tanaka, H. Harima, A. Yanase, J. Phys. Soc. Jpn. 67 (1998) 1342.
[15] A. Sekiyama, H. Fujiwara, S. Imada, S. Suga, H. Eisaki, S.I. Uchida, K. Takegahara, H. Harima, Y. Saitoh, I.A. Nekrasov, G. Keller, D.E. Kondakov, A.V. Kozhevnikov, Th. Pruschke, K. Held, D. Vollhardt, V.I. Anisimov, Phys. Rev. Lett. 93 (2004) 156402.
[16] Y. Aiura, F. Iga, Y. Nishihara, H. Ohnuki, H. Kato, Phys. Rev. B: Condens. Matter 47 (1993) 6732.
[17] I.H. Inoue, I. Hase, Y. Aiura, A. Fujimori, Y. Haruyama, T. Maruyama, Y. Nishihara, Phys. Rev. Lett. 74 (1995) 2539.
[18] S. Tanuma, C.J. Powell, D.R. Penn, Surf. Sci. 192 (1987) L849.
[19] Y. Saitoh, Y. Fukuda, Y. Takeda, H. Yamagami, S. Takahashi, Y. Asano, T. Hara, K. Shirasawa, M. Takeuchi, T. Tanakad, H. Kitamura, J. Synchrotron Rad. 19 (2012) 388.
[20] S. Yamamoto, Y. Senba, T. Tanaka, H. Ohashi, T. Hirono, H. Kimura, M. Fujisawa, J. Miyawaki, A. Harasawa, T. Seike, S. Takahashi, N. Nariyama, T. Matsushita, M. Takeuchi, T. Ohata, Y. Furukawa, K. Takeshita, S. Goto, Y. Harada, S. Shin, H. Kitamura, A. Kakizaki, M. Oshima, I. Matsuda, J. Synchrotron Rad. 21 (2014) 352.
[21] V.N. Strocov, M. Kobayashi, X. Wang, L.L. Lev, J. Krempasky, V.V. Rogalev, T. Schmitt, C. Cancellieri, M.L. Reinle-Schmitt, Synchr. Rad. News 27 (2014) 24.
[22] J. Avila, M.C. Asensio, Synchr. Rad. News 27 (2014) 31–40.
[23] Angle-resolved photoemission spectroscopy, Synchrotron Rad. News 25(2012) 2–40.
[24] A. Kimura, J. Vac. Soc. Jpn. 57 (7) (2014) 249.
[25] S. Suga, A. Shigemoto, A. Sekiyama, S. Imada, A. Yamasaki, A. Irizawa, S. Kasai, Y. Saitoh, T. Muro, N. Tomita, K. Nasu, H. Eisaki, Y. Ueda, Phys. Rev. B: Condens. Matter 70 (2004) 155106.
[26] A. Sekiyama, S. Kasai, M. Tsunekawa, Y. Ishida, M. Sing, A. Irizawa, A. Yamasaki, S. Imada, T. Muro, Y. Saitoh, Y. Onuki, T. Kimura, Y. Tokura, S. Suga, Phys. Rev. B: Condens. Matter 70 (2004), 060506(R).
[27] M. Tsunekawa, A. Sekiyama, S. Kasai, S. Imada, H. Fijiwara, T. Muro, Y. Onose, Y. Tokura, S. Suga, New J. Phys. 10 (2008) 073005.
[28] S.-K. Mo, H.-D. Kim, J.D. Denlinger, J.W. Allen, J.-H. Park, A. Sekiyama, A. Yamasaki, S. Suga, Y. Saitoh, T. Muro, P. Metcalf, Phys. Rev. B: Condens. Matter 74 (2006) 165101;
S.-K. Mo, J.D. Denlinger, H.-D. Kim, H.-H. Park, J.W. Allen, A. Sekiyama, A. Yamasaki, K. Kadono, S. Suga, Y. Saitoh, T. Muro, P. Metcalf, G. Keller, K. Held, V. Eyert, V.I. Anisimov, D. Vollhardt, Phys. Rev. Lett. 90 (2003) 186403.
[29] M. Yano, A. Sekiyama, H. Fujiwara, Y. Amano, S. Imada, T. Muro, M. Yabashi, K. Tamasaku, A. Higashiya, T. Ishikawa, Y. Onuki, S. Suga, Phys. Rev. B: Condens. Matter 77 (2008) 035118.
[30] T. Ohkochi, S. Fujimori, H. Yamagami, T. Okane, Y. Saitoh, A. Fujimori, Y. Haga, E. Yamamoto, Y. Ōnuki, Phys. Rev. B: Condens. Matter 78 (2008) 165110.
[31] T. Muro, Y. Kato, T. Matsushita, T. Kinoshita, Y. Watanabe, H. Okazaki, T. Yokoya, A. Sekiyama, S. Suga, J. Synchrton Rad. 18 (2011) 879.
[32] H. Fujiwara, T. Kiss, Y.K. Wakabayashi, Y. Nishitani, T. Mori, Y. Nakata, S. Kitayama, K. Fukushima, S. Ikeda, H. Fuchimoto, Y. Minowa, S.-K. Mo, J. Denlinger, J.W. Allen, P. Metcalf, M. Imai, K. Yoshimura, S. Suga, T. Muro, A. Sekiyama, J. Synchrotron Rad. 22 (2015) 776.
[33] J.J. Yeh, I. Lindau, Atom. Data Nucl. Data Tables 32 (1985) 1.
[34] T. Hara, M. Yabashi, T. Tanaka, T. Bizen, S. Goto, X.M. Maréchal, T. Seike, K. Tamasaku, T. Ishikawa, H. Kitamura, Rev. Sci. Instrum. 73 (2002) 1125.
[35] T. Mori, S. Kitayama, Y. Kanai, S. Naimen, H. Fujiwara, A. Higashiya, K. Tamasaku, A. Tanaka, K. Terashima, S. Imada, A. Yasui, Y. Saitoh, K. Yamagami, K. Yano, T. Matsumoto, T. Kiss, M. Yabashi, T. Ishikawa, S. Suga, Y. Onuki, T. Ebihara, A. Sekiyama, J. Phys. Soc. Jpn. 83 (2014) 123702.
[36] S. Suga, A. Sekiyama, H. Fujiwara, Y. Nakatsu, T. Miyamachi, S. Imada, P. Baltzer, S. Niitaka, H. Takagi, K. Yoshimura, M. Yabashi, K. Tamasaku, A. Higashiya, T. Ishikawa, New J. Phys. 11 (2009) 073025.
[37] S. Suga, A. Sekiyama, H. Fujiwara, Y. Nakatsu, J. Yamaguchi, M. Kimura, K. Murakami, S. Niitaka, H. Takagi, M. Yabashi, K. Tamasaku, A. Higashiya, T. Ishikawa, I. Nekrasov, J. Phys. Soc. Jpn. 79 (2010) 044711.
[38] S. Suga, S. Itoda, A. Sekiyama, H. Fujiwara, S. Komori, S. Imada, M. Yabashi, K. Tamasaku, A. Higashiya, T. Ishikawa, M. Shang, T. Fujikawa, Phys. Rev. B: Condens. Matter 86 (2012) 035146.
[39] A.X. Gray, C. Papp, S. Ueda, B. Balke, Y. Yamashita, L. Plucinski, J. Minár, J. Braun, E.R. Ylvisaker, C.M. Schneider, W.E. Pickett, H. Ebert, K. Kobayashi, C.S. Fadley, Nat. Mater. 10 (2011) 759.
[40] S. Tanuma, C.J. Powell, D.R. Penn, Surf. Interface Anal. 43 (2011) 689.
[41] M. Kimura, H. Fujiwara, A. Sekiyama, J. Yamaguchi, K. Kishimoto, H. Sugiyama, G. Funabashi, S. Imada, S. Iguchi, Y. Tokura, A. Higashiya, M. Yabashi, K. Tamasaku, T. Ishikawa, T. Ito, S. Kimura, S. Suga, J. Phys. Soc. Jpn. 79 (2010) 064710.
[42] Y. Nakatsu, A. Sekiyama, S. Imada, Y. Okamoto, S. Niitaka, H. Takagi, A. Higashiya, M. Yabashi, K. Tamasaku, T. Ishikawa, S. Suga, Phys. Rev. B: Condens. Matter 83 (2011) 115120.
[43] F. Rodolakis, B. Mansart, E. Papalazarou, S. Gorovikov, P. Vilmercati, L. Petaccia, A. Goldoni, J.P. Rueff, S. Lupi, P. Metcalf, M. Marsi, Phys. Rev. Lett. 102 (2009) 066805.
[44] H. Fujiwara, A. Sekiyama, S.-K. Mo, J.W. Allen, J. Yamaguchi, G. Funabashi, S. Imada, P. Metcalf, A. Higashiya, M. Yabashi, K. Tamasaku, T. Ishikawa, S. Suga, Phys. Rev. B: Condens. Matter 84 (2011) 075117.
[45] M.Z. Hasan, C.L. Kane, Rev. Mod. Phys. 82 (2010) 3045.
[46] L. Plucinski, G. Mussler, J. Krumrain, A. Herdt, S. Suga, D. Grützmacher, C.M. Schneider, Appl. Phys. Lett. 98 (2011) 222503.
[47] G. Ghiringhelli, K. Larsson, N.B. Brookes, Rev. Sci. Instrum. 70 (1999) 4225.
[48] J. Kirschner, S. Suga, Solid State Commun. 64 (1987) 997.
[49] H.P. Oepen, K. Hünlich, J. Kirschner, A. Eyers, F. Schäfers, G. Schönhense, U. Heinzmann, Phys. Rev. B: Condens. Matter 31 (1985) 6846.
[50] D. Venus, J. Garbe, S. Suga, C. Schneider, J. Kirschner, Phys. Rev. B: Condens. Matter 34 (1986) 8435.
[51] Y. Saitoh, T. Matsushita, S. Imada, H. Daimon, S. Suga, J. Fujii, K. Shimada, A. Kakizaki, K. Ono, M. Fujisawa, T. Kinoshita, T. Ishii, Phys. Rev. B: Condens. Matter 52 (1995) R11549.
[52] D. Yu, C. Math, M. Meier, M. Escher, G. Rangelov, M. Donath, Sur. Sci. 601 (2007) 5803.
[53] F. Lofink, S. Hankemeier, R. Froömter, J. Kirschner, H.P. Oepen, Rev. Sci. Instrum. 83 (2012) 023708.
[54] T. Okuda, K. Miyamoto, H. Miyahara, K. Kuroda, A. Kimura, H. Namatame, M. Taniguchi, Rev. Sci. Instrum. 82 (2011) 103302.
[55] A. Winkelmann, D. Hartung, H. Engelhard, C.-T. Chiang, J. Kirschner, Rev. Sci. Instrum. 79 (2008) 083303.
[56] S. Suga, K. Sakamoto, T. Okuda, K. Miyamoto, K. Kuroda, A. Sekiyama, J. Yamaguchi, H. Fujiwara, A. Irizawa, T. Ito, S. Kimura, T. Balashov, W. Wulfhekel, S. Yeo, F. Iga, S. Imada, J. Phys. Soc. Jpn. 83 (2014) 014705.
[57] C. Thiede, C. Langenkämper, K. Shirai, A. Schmidt, T. Okuda, M. Donath, Phys. Rev. Appl. 1 (2014) 054003.
[58] R. Jungblut, Ch. Roth, F.U. Hillebrecht, E. Kisker, Surf. Sci. 269/270 (1992) 615.
[59] T. Okuda, K. Miyamoto, A. Kimura, H. Namatame and M. Taniguchi, J. Electr. Rel. Phenom. to be published.
[60] S. Souma, K. Kosaka, T. Sato, M. Komatsu, A. Takayama, T. Takahashi, M. Kriener, K. Segawa, Y. Ando, Phys. Rev. Lett. 106 (2011) 216803.
[61] F. Hadjarab, J.L. Erskine, J. Electr. Spectrosc. Relat. Phenom. 36 (1985) 227.
[62] M. Kotsugi, W. Kuch, F. Offi, L.I. Chelaru, J. Kirschner, Rev. Sci. Instrum. 74 (2003) 2754.
[63] A. Oelsner, O. Schmidt, M. Schicketanz, M. Klais, G. Schönhense, V. Mergel, O. Jagutzki, H. Schmidt-Böcking, Rev. Sci. Instrum. 72 (2001) 3968.
[64] R. van Gastel, I. Sikharulidze, S. Schramm, J. Abrahams, B. Poelsema, R. Tromp, S. van der Molen, Ultramicroscopy 110 (2009) 33.
[65] B. Krömker, M. Escher, D. Funnemann, D. Hartung, H. Engelhard, J. Kirschner, Rev. Sci. Instrum. 79 (2008) 053702.
[66] M. Escher, N. Weber, M. Merkel, C. Ziethen, P. Bernhard, G. Schönhense, S. Schmidt, F. Forster, F. Reinert, et al., J. Phys.: Condens. Matter 17 (2005) S1329.
[67] A. Winkelmann, C. Tusche, A.A. Ünal, M. Ellguth, J. Henk, J. Kirschner, New J. Phys. 14 (2012) 043009.
[68] N.A. Cherepkov, G. Schönhense, Europhys. Lett. 24 (1993) 79.
[69] V.N. Strocov, R. Claessen, F. Aryasetiawan, P. Blaha, P.O. Nilsson, Phys. Rev. B: Condens. Matter 66 (2002) 195104.
[70] A.A. Ünal, A. Winkelmann, C. Tusche, F. Bisio, M. Ellguth, C.-T. Chiang, J. Henk, J. Kirschner, Phys. Rev. B: Condens. Matter 86 (2012) 125447.
[71] C. Mathieu, N. Barrett, J. Rault, Y.Y. Mi, B. Zhang, W.A. de Heer, C. Berger, E.H. Conrad, O. Renault, Phys. Rev. B: Condens. Matter 83 (2011) 235436.
[72] C. Wiemann, M. Patt, I.P. Krug, N.B. Weber, M. Escher, M. Merkel, C.M. Schneider, e-J. Surf. Sci. Nanotech. 9 (2011) 395.
[73] D. Funnemann, M. Escher, Nr. EP 1 559 126 B1 (2007).
[74] N.B. Weber, M. Escher, M. Merkel, A. Oelsner, G. Schönhense, J. Phys: Conf. Ser. 100 (2008) 072031.
[75] A. Locatelli, E. Bauer, J. Phys.: Condens. Matter 20 (2008) 093002.
[76] K.R. Knox, A. Locatelli, M.B. Yilmaz, D. Cvetko, T.O. Mente s, M.Á. Niño, P. Kim, A. Morgante, R.M. Osgood, Phys. Rev. B: Condens. Matter 84 (2011) 115401.
[77] R.M. Tromp, Y. Fujikawa, J.B. Hannon, A.W. Ellis, A. Berghaus, O. Schaff, J. Phys.: Condens. Matter 21 (2009) 314007.
[78] J. Henk, A. Ernst, P. Bruno, Phys. Rev. B: Condens. Matter 68 (2003) 165416.
[79] M. Hoesch, M. Muntwiler, V.N. Petrov, M. Hengsberger, L. Patthey, M. Shi, M. Falub, T. Greber, J. Osterwalder, Phys. Rev. B: Condens. Matter 69 (2004) 241401.
[80] G. Schönhense, A. Oelsner, O. Schmidt, G. Fecher, V. Mergel, O. Jagutzki, H. Schmidt-Böcking, Surf. Sci. 480 (2001) 180.
[81] S.V. Chernov, K. Medjanik, C. Tusche, D. Kutnyakhov, S.A. Nepijko, A. Oelsner, J. Braun, J. Minár, S. Borek, H. Ebert, H.J. Elmers, J. Kirschner, G. Schönhense, Ultramicroscopy (2015) (Submitted).
[82] C. Wiemann, M. Patt, S. Cramm, M. Escher, M. Merkel, A. Gloskovskii, S. Thiess, W. Drube, C.M. Schneider, Appl. Phys. Lett. 100 (2012) 223106.
[83] R. Waser, R. Dittmann, G. Staikov, K. Szot, Adv. Mater. 21 (2009) 2632.
[84] R. Tromp, W. Wan, S. Schramm, Ultramicroscopy 119 (2012) 33.
[85] G. Schönhense, K. Medjanik, C. Tusche, M. de Loos, B. van der Geer, M. Scholz, F. Hieke, N. Gerken, J. Kirschner, W. Wurth, Ultramicroscopy (2015) (Submitted).
[86] C. Tusche, M. Ellguth, A.A. Ünal, C.-T. Chiang, A. Winkelmann, A. Krasyuk, M. Hahn, G. Schönhense, J. Kirschner, Appl. Phys. Lett. 99 (2011) 032505.

[87] M. Kolbe, P. Lushchyk, B. Petereit, H.J. Elmers, G. Schönhense, A. Oelsner, C. Tusche, J. Kirschner, Phys. Rev. Lett. 107 (2011) 207601.
[88] D. Vasilyev, C. Tusche, F. Giebels, H. Gollisch, R. Feder, J. Kirschner, J. Electron Spectrosc. Relat. Phenom. 199 (2015) 10.
[89] J. Kirschner, R. Feder, Phys. Rev. Lett. 42 (1979) 1008.
[90] D. Kutnyakhov, P. Lushchyk, A. Fognini, D. Perriard, M. Kolbe, K. Medjanik, E. Fedchenko, S. Nepijko, H. Elmers, G. Salvatella, C. Stieger, R. Gort, T. Bähler, T. Michlmayer, Y. Acremann, A. Vaterlaus, F. Giebels, H. Gollisch, R. Feder, C. Tusche, A. Krasyuk, J. Kirschner, G. Schönhense, Ultramicroscopy 130 (2013) 63.
[91] J. Kirschner, F. Giebels, H. Gollisch, R. Feder, Phys. Rev. B: Condens. Matter 88 (2013) 125419.
[92] M. Hahn, G. Schönhense, E.A. Jorge, M. Jourdan, Appl. Phys. Lett. 98 (2011) 232503.
[93] C.M. Cacho, S. Vlaic, M. Malvestuto, B. Ressel, E.A. Seddon, F. Parmigiani, Rev. Sci. Instrum. 80 (2009) 043904.
[94] C. Jozwiak, J. Graf, G. Lebedev, N. Andresen, A.K. Schmid, A.V. Fedorov, F. El Gabaly, W. Wan, A. Lanzara, Z. Hussain, Rev. Sci. Instrum. 81 (2010) 053904.
[95] W. Kuch, R. Frömter, J. Gilles, D. Hartmann, C. Ziethen, C.M. Schneider, G. Schönhense, W. Swiech, J. Kirschner, Surf. Rev. Lett. 05 (1998) 1241.
[96] A. Krasyuk, A. Oelsner, S. Nepijko, A. Kuksov, C. Schneider, G. Schönhense, Appl. Phys. A: Mater. Sci. Process. 76 (2003) 863.
[97] J. Vogel, W. Kuch, M. Bonfim, J. Camarero, Y. Pennec, F. Offi, K. Fukumoto, J. Kirschner, A. Fontaine, S. Pizzini, Appl. Phys. Lett. 82 (2003) 2299.
[98] N. Rougemaille, A.K. Schmid, Eur. Phys. J. Appl. Phys. 50 (2010) 20101.
[99] C.-T. Chiang, A. Winkelmann, J. Henk, F. Bisio, J. Kirschner, Phys. Rev. B: Condens. Matter 85 (2012) 165137.
[100] C. Tusche, M. Ellguth, A. Krasyuk, A. Winkelmann, D. Kutnyakhov, P. Lushchyk, K. Medjanik, G. Schönhense, J. Kirschner, Ultramicroscopy 130 (2013) 70.
[101] Y.A. Mamaev, L.G. Gerchikov, Y.P. Yashin, D.A. Vasiliev, V.V. Kuzmichev, V.M. Ustinov, A.E. Zhukov, V.S. Mikhrin, A.P. Vasiliev, Appl. Phys. Lett. 93 (2008) 081114.
[102] D. Kutnyakhov, H.J. Elmers, G. Schöonhense, C. Tusche, S. Borek, J. Braun, J. Minár, H. Ebert, Phys. Rev. B: Condens. Matter 91 (2015) 014416.
[103] R. Feder, J. Phys. C: Solid State Phys. 14 (1981) 2049.
[104] G. Schönhense, K. Medjanik, H.-J. Elmers, J. Electron Spectr. Rel. Phenom. 200 (2015) 95.
[105] C. Jozwiak, A. Lanzara, Z. Hussain, Synchrotron Rad. News 25 (2012) 32.
[106] J. Kirschner, R. Feder, J.F. Wendelken, Phys. Rev. Lett. 47 (1981) 614.
[107] U. Heinzmann, J. Phys. B: At. Mol. Phys. 11 (1978) 399.
[108] E. Kisker, Rev. Sci. Instrum. 53 (1982) 1137.
[109] L.G. Gray, M.W. Hart, F.B. Dunning, G.K. Walters, Rev. Sci. Instrum. 55 (1984) 88.
[110] D. Tillmann, R. Thiel, E. Kisker, Z. Physik B—Condens. Matter 77 (1989) 1.
[111] S. Qiao, A. Kimura, A. Harasawa, M. Sawada, J.-G. Chung, A. Kakizaki, Rev. Sci. Instrum. 68 (1997) 4390.
[112] F.U. Hillebrecht, R.M. Jungblut, L. Wiebusch, C. Roth, H.B. Rose, D. Knabben, C. Bethke, N.B. Weber, S. Manderla, et al., Rev. Sci. Instrum. 73 (2002) 1229.
[113] V.N. Petrov, V.V. Grebenshikov, A.N. Andronov, P.G. Gabdullin, A.V. Maslevtcov, Rev. Sci. Instrum. 78 (2007) 025102.